USE OF BAFFLES IN CAVITY FLOW FOR THE SUPPRESSION OF THERMAL OSCILLATIONS UNDER MICROGRAVITY

MARY C. HO AND B. RAMASWAMY

Department of Mechanical Engineering and Materials Science, Rice University, Houston, Texas 77251-1892, USA

ABSTRACT

The quality of crystals grown from melt depends on the flow field in the melt. To simulate melt conditions, a finite element analysis is performed on flow in a heated cavity under the driving forces of natural convection, thermocapillary effects and rotation. In addition, the gravity field is modulated to simulate a microgravitational environment. The purpose for conducting this research is to determine whether the use of baffles can effectively reduce convection and suppress temperature oscillations. The results show that the baffle is able to suppress convection and reduce the amplitude of the temperature oscillations when placed perpendicular to the modulation direction. Under crystal and crucible rotation, the results with and without baffles are similar. In all cases, baffles did not induce temperature oscillations. From this study, it can be concluded that the effects of baffles on the flow behaviour depends greatly on the direction of gravity modulation and frequency.

KEY WORDS Cavity flow Crystal growth Czochralski Finite element Navier–Stokes Microgravity

NOMENCLATURE

a	radius of the crystal,	T	temperature,
F_m	mean value of the gravitational acceleration,	ΔT	temperature difference,
		T_c	cold wall temperature,
g	gravitational acceleration,	T_h	hot wall temperature,
$D_{\alpha\beta}$	divergence matrix,	T_m	mean temperature,
H	height of cavity,	u	velocity component in x-direction,
$K_{\alpha\beta\gamma}$	convection matrix,	u_α	x-component nodal value of velocity,
L	width of cavity,	$\tilde{u}, \hat{u}$	intermediate velocity,
$M_{\alpha\beta}$	mass matrix,	v	velocity component in y-direction,
n_i	normal vector,	v_α	y-component nodal value of velocity,
p	nondimensional pressure,	$\tilde{v}, \hat{v}$	intermediate velocity,
p_α	node value of pressure,	w	velocity component in θ-direction,
R	radius of cylindrical cavity,	w_α	θ-component nodal value of velocity,
$S_{\alpha\beta}$	diffusion matrix of the momentum equation,	(x, y)	Cartesian coordinates,
		(r, z, θ)	Cylindrical coordinates.
S_1	source term of the momentum equation in x direction,		
S_2	source term of the momentum equation in y direction,	*Greek letters*	
Δt	time increment,	α	thermal diffusivity,
		β	thermal expansion coefficient,

η gravity modulation amplitude,
μ coefficient of viscosity,
ν coefficient of kinematic viscosity,
ω nondimensionalized frequency, vorticity,
Ω bounded domain of R^2,
Φ_α shape functions,
ϕ phase angle,
ψ streamfunction,
ρ fluid density,
σ surface tension.

Subscripts

$\overset{\centerdot}{}$ derivative w.r.t. r,
z derivative w.r.t. z,
α, β, γ nodal number.

Superscripts

n nth time steps,

*   refers to non-dimensional values,
~   intermediate value,
─   intermediate value.

Non-dimensional numbers

AR aspect ratio, $AR = \dfrac{R}{H}$ and $\dfrac{H}{L}$,

Ma Marangoni number, $Ma = \dfrac{\partial \sigma}{\partial T^*} \dfrac{\Delta T^* L}{\mu \alpha}$,

Gr Grashof number, $Gr = \dfrac{g\beta \Delta T^* L^3}{\nu^2}$,

Pr Prandtl number, $Pr = \dfrac{\nu}{\alpha}$,

Ra Rayleigh number, $Ra = \dfrac{g\beta \Delta T^* L^3}{\nu \alpha}$,

Re Reynolds number, $Re = \dfrac{r\omega}{\nu}$.

INTRODUCTION

Crystals have many applications in science and engineering. For example, semiconductor crystals are used for lasers and integrated circuits. The effectiveness and performance of these devices depend largely on the quality of the crystal used. Thus, the importance of producing the right size and quality of crystals is easy to recognize. Before one can learn to control the growth of a crystal, one must first have a good grasp of the fundamental principles and parameters that govern the growth process. This study is focused on the growth of large single crystals. The most common growth-from-melt technique is the Czochralski method. Basically, the Czochralski method of crystal growth utilizes the melt of a substance as a nutrient for the seed to be grown. The melt is contained in a cylindrical crucible, and its temperature is maintained at the melting point of the material by heating the bottom of the crucible. The seed is attached to the lower end of a pull rod, which is lowered into the melt, then slowly rotated and pulled up as the liquid metal solidifies around it. Consequently, one could assume that the governing parameters include aspect ratio, rotation rate, pulling rate, and the magnitude of the temperature gradient between the top and bottom of the crucible. The key to improving crystal quality is to manipulate and optimize these parameters to produce the most perfectly formed crystal.

The Czochralski configuration can be simplified and modelled as viscous flow in an enclosed cavity that is heated at the bottom. Since the melt is usually in the form of a molten metal, a low Prandtl number is used to represent the fluid. Under normal terrestrial conditions, this setup would create an unstable density gradient, resulting in the circular motion of the fluid. Consequently, heat is transferred through conduction as well as through the energy transported by the circulation of the fluid. This is a typical Rayleigh–Bernard convection problem.

In an effort to improve the quality and size of crystals, scientists have explored the possibility of processing in space. Although gravity is not exactly zero on the shuttle, it is considerably less than on Earth. In Spacelab, for instance, the acceleration of gravity can reach about 1×10^{-3}–1×10^{-4} the amount of earth gravity. Consequently, the space environment causes a significant reduction in sedimentation and buoyancy driven convection. These advantages help provide the ideal setting and conditions for crystal growth. However, because the g-values are so low, any seemingly small excitation in the vicinity would prove to be significant. Furthermore, other forces which dominate in a low gravity environment may be present to change the behaviour

of the flow. For example, surface tension does not depend on gravity, so surface tension forces should be considered in any analysis done in microgravity. The gravity field found in the space environment can be separated into two components: the mean component and the oscillatory component[4]. The oscillatory component comes from fluctuations in the gravity field in space, and they are called g-jitters. G-jitters are usually caused by crew motion, spacecraft manoeuvres, extra-vehicular activities, and machine operation on board the spacecraft, and can therefore act in any direction. Since the direction of gravity with respect to the temperature gradient has a significant impact on the resulting flow regime, it is important to examine the effects of jitter direction on the flow. Gresho and Sani performed a linear analysis on the effects of gravity modulation on the resulting critical Rayleigh number[2]. Jue et $al.$ studied the effects of oscillatory flow in a cavity using a finite element splitting scheme[3]. The results of their studies prove that the frequency and direction of gravity modulation have a significant effect on the stability of the flow.

Besides changing the environment to improve growth, literature shows that modifications to the growth configuration can also be effective. It has been suggested that the use of a baffle in the vicinity of the melt would reduce convection as well as suppress thermal oscillations. Brice and Whiffen performed experiments in which vertical and horizontal flat plate baffles were placed in the crucible during the growth of a crystal from a zinc tungstate melt[6]. They showed in their experiment that permeable horizontal baffles produced the best results. In addition, Sahai, Williamson, and Overfelt performed numerical analyses on the effects of placement and number of baffles on convection in microgravity[5]. They found that baffles reduced buoyancy-induced convection considerably. This investigation combines some of the possible configurations and tactics discussed to determine their effects on the flow behaviour through numerical simulation, and make some conclusions as to how they might influence the conditions under which a crystal would be grown.

The objective of this study is to achieve a better understanding of how to improve the conditions under which a crystal is grown by controlling mass transport. In particular, this study explores the use of baffles in a fluid filled cavity for the purpose of controlling convection and reducing temperature oscillations. The cases analysed deal with the combined effect of natural convection, thermocapillary convection, and forced convection on the proposed configuration. Furthermore, all cases considered are simulated under micro-gravitational conditions for different frequencies and directions of g-jitters.

GOVERNING EQUATIONS

The governing equations for the problems investigated are the transient form of the Navier–Stokes equations. The equations in this formulation are derived from the principles of the conservation of mass, momentum, and energy. In this study, the primitive variables are chosen to formulate the equations, and the stream function is used to display the results. The equations for a two-dimensional axisymmetric case expressed in r, z, and θ are shown below. Although the actual problem is two dimensional, the θ component of the velocity must be included in the calculations to account for the effects of rotation.

Continuity

$$\frac{1}{r}\frac{\partial}{\partial r}(ru) + \frac{\partial v}{\partial z} = 0 \quad \text{in } \Omega \tag{1}$$

r-Momentum

$$\frac{\partial u}{\partial t} + u\frac{\partial u}{\partial r} + v\frac{\partial u}{\partial z} - \frac{w^2}{r} = -\frac{1}{\rho}\frac{\partial p}{\partial z} + v\left(\nabla^2 u - \frac{u}{r^2}\right) + \beta g(T - T_s) \quad \text{in } \Omega \tag{2}$$

z-Momentum

$$\frac{\partial v}{\partial t} + u\frac{\partial v}{\partial r} + v\frac{\partial v}{\partial z} = -\frac{1}{\rho}\frac{\partial p}{\partial r} + \nu\nabla^2 v + \beta g(T - T_s) \quad \text{in } \Omega \tag{3}$$

θ-Momentum

$$\frac{\partial w}{\partial t} + u\frac{\partial w}{\partial r} + v\frac{\partial w}{\partial z} + \frac{uw}{r} = \nu\left(\nabla^2 w - \frac{w}{r^2}\right) \quad \text{in } \Omega \tag{4}$$

Energy

$$\frac{\partial T}{\partial t} + u\frac{\partial T}{\partial r} + v\frac{\partial T}{\partial z} = \alpha\nabla^2 T \quad \text{in } \Omega \tag{5}$$

The non-dimensionalization scales and parameters used are:

$$r^* = \frac{r}{R} \qquad z^* = \frac{z}{R}$$

$$t^* = \frac{t}{\alpha/R^2} \qquad u^* = \frac{u}{\alpha/R^2}$$

$$v^* = \frac{v}{\alpha/R^2} \qquad T^* = \frac{(T - T_m)}{(T_h - T_c)}$$

where R is the radius of the cylinder and α is the thermal diffusivity. The aspect ratio for this problem can be defined as $AR = R/H$, where R is the radius of the cylinder, and H is the height of the cylinder. The non-dimensionalized form of the equations can now be formed.

Continuity

$$\frac{\partial u^*}{\partial r^*} + \frac{u^*}{r^*} + \frac{\partial v^*}{\partial z^*} = 0 \quad \text{in } \Omega \tag{6}$$

r-Momentum

$$\frac{\partial u^*}{\partial t^*} + \left(u^*\frac{\partial u^*}{\partial r^*} + v^*\frac{\partial u^*}{\partial z^*}\right) - \frac{w^{*2}}{r^*} = -\frac{\partial p^*}{\partial r^*} + Pr\left[\frac{1}{r^*}\frac{\partial}{\partial r^*}\left(r^*\frac{\partial u^*}{\partial r^*}\right) + \frac{\partial^2 u^*}{\partial z^{*2}} - \frac{u^*}{r^{*2}}\right] + S_1 \quad \text{in } \Omega \tag{7}$$

z-Momentum

$$\frac{\partial v^*}{\partial t^*} + \left(u^*\frac{\partial v^*}{\partial r^*} + v^*\frac{\partial v^*}{\partial z^*}\right) = -\frac{\partial p^*}{\partial z^*} + Pr\left[\frac{1}{r^*}\frac{\partial}{\partial r^*}\left(r^*\frac{\partial v^*}{\partial r^*}\right) + \frac{\partial^2 v^*}{\partial z^{*2}}\right] + S_2 \cdot \quad \text{in } \Omega \tag{8}$$

θ-Momentum

$$\frac{\partial w^*}{\partial t^*} + \left(u^*\frac{\partial w^*}{\partial r^*} + v^*\frac{\partial w^*}{\partial z^*}\right) + \frac{u^* w^*}{r^*} = Pr\left[\frac{1}{r^*}\frac{\partial}{\partial r^*}\left(r^*\frac{\partial w^*}{\partial r^*}\right) + \frac{\partial^2 w^*}{\partial z^{*2}}\right] - Pr\left(\frac{w^*}{r^{*2}}\right) \quad \text{in } \Omega \tag{9}$$

Energy

$$\frac{\partial T^*}{\partial t^*} + \left(u^*\frac{\partial T^*}{\partial r^*} + v^*\frac{\partial T^*}{\partial z^*}\right) = \left(\frac{\partial^2 T^*}{\partial r^{*2}} + \frac{\partial^2 T^*}{\partial z^{*2}}\right) \quad \text{in } \Omega \tag{10}$$

where

$$S_1 = S_2 = RaPrT^*[F_m + \eta\cos(\omega t + \phi)] \tag{11}$$

The terms S_1 and S_2 represent the modulated body force, and their subscripts denote the direction of modulation. In the same equation, η is the amplitude of oscillation, ω is the frequency, and ϕ is the phase angle. The sinusoidal oscillation is applied here also, so ϕ is zero. The

non-dimensionalized parameters Pr and Ra are defined as:

$$Pr = \frac{\nu}{\alpha}$$

$$Ra = \frac{g\beta\Delta T^* R^3}{\nu\alpha}$$

For simplicity, the asterisks denoting non-dimensionalization will be dropped after this point. The fluid considered in each case is assumed to be two dimensional and incompressible. As such, the density should be constant and neglected. However, a density gradient does exist due to the temperature gradient imposed on the cavity. Therefore, the convention is to apply the Boussinesq assumption, which accounts for the density changes in the body force term. The density variation is then defined to be:

$$\rho = \rho_0(1 - \beta(T - T_o)) \tag{12}$$

in which β represents the thermal expansion ratio. When surface tension, σ, due to temperature gradient is included in the analysis, the surface tension is defined as:

$$\sigma = \sigma_o(1 - \gamma(T - T_o)) \tag{13}$$

Viscous dissipation and radiation are both neglected. The initial conditions are given in the form of

$$u = v = w = \theta = 0 \quad \text{at } t = 0 \tag{14}$$

For boundary conditions, the velocities are assumed to be zero at all solid boundaries, except when rotation is involved, and no slip at the free surface. The bottom of the cavity is heated, and the top of the cavity is cooled. Diagrams defining the problem and boundary conditions for the rectangular cavity and the cylindrical cavity are shown in *Figure 1*. *Figure 1a* shows the rectangular cavity problem, and *Figure 1b* shows the cylindrical cavity geometry, where a is the radius of the crystal. The Marangoni number shown in the boundary equation for the free surface represents the ratio of the change in surface tension to viscous force:

$$Ma = \frac{\partial\sigma}{\partial T^*} \frac{\Delta T^* L}{\mu\alpha}$$

and the Reynolds number represents the magnitude of crystal or crucible rotation, and can be defined as:
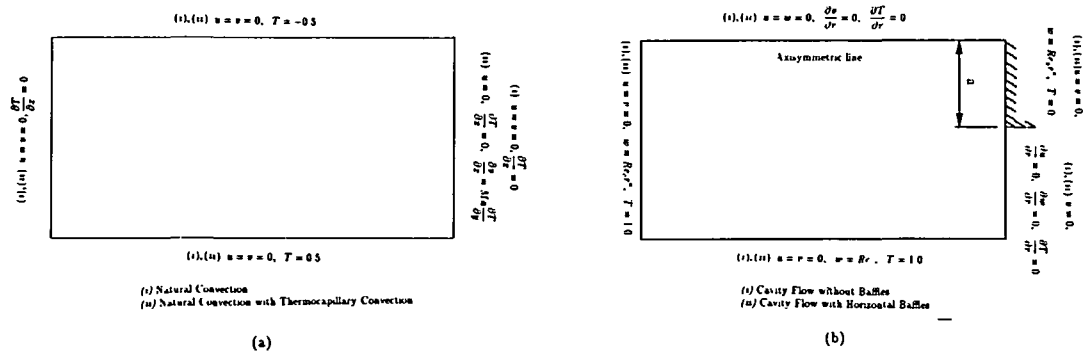
$$Re = \frac{r^2\omega}{\nu}$$

Figure 1 Problem definition: (a) rectangular cavity, (b) cylindrical cavity

The crystal radius is used to calculate the Reynolds number for crystal rotation, and the crucible radius is used to calculate the Reynolds number for crucible rotation.

NUMERICAL PROCEDURE

Time discretization

The temporal variables are discretized using a semi-implicit time-splitting scheme. The advection terms are advanced using the explicit Adams–Bashforth method, and the viscous terms are advanced using the implicit Euler scheme. The use of the implicit method enables one to use a large time step, while the explicit method reduces the required storage space. The fractional step method is used to solve the equations of fluid motion. Basically, the procedure is divided into four steps:

Step 1

In this step, the pressure and viscous terms are dropped from the r and z momentum equations, and an intermediate velocity field, $\bar{u}^{n+1}$ and $\bar{v}^{n+1}$, are computed from the convective terms. The resulting equations written in the form of the Adams–Bashforth scheme are as follows:

$$\bar{u}^{n+1} = u^n - \Delta t\left[\frac{3}{2}\left(u^n\frac{\partial u^n}{\partial r}\right) - \frac{1}{2}\left(u^{n-1}\frac{\partial u^{n-1}}{\partial r}\right)\right] - \Delta t\left[\frac{3}{2}\left(v^n\frac{\partial u^n}{\partial z}\right) - \frac{1}{2}\left(v^{n-1}\frac{\partial u^{n-1}}{\partial z}\right)\right]$$

$$+ \Delta t\left[\frac{3}{2}\left(\frac{(w^n)^2}{r}\right) - \frac{1}{2}\left(\frac{(w^{n-1})^2}{r}\right)\right] + \Delta t S_1 \tag{15}$$

$$\bar{v}^{n+1} = v^n - \Delta t\left[\frac{3}{2}\left(u^n\frac{\partial v^n}{\partial r}\right) - \frac{1}{2}\left(u^{n-1}\frac{\partial v^{n-1}}{\partial r}\right)\right] - \Delta t\left[\frac{3}{2}\left(v^n\frac{\partial v^n}{\partial z}\right) - \frac{1}{2}\left(v^{n-1}\frac{\partial v^{n-1}}{\partial z}\right)\right] + \Delta t S_2 \tag{16}$$

Step 2

In this step, new intermediate velocity values are determined by including the viscous terms, which are solved using the implicit Euler scheme. These new velocities are denoted by $\tilde{u}^{n+1}$ and $\tilde{v}^{n+1}$.

$$\tilde{u}^{n+1} = \bar{u}^{n+1} - \Delta t Pr\left[\frac{1}{r}\left(r\frac{\partial\tilde{u}^{n+1}}{\partial r}\right) + \frac{\partial^2\tilde{u}^{n+1}}{\partial z^2} + \frac{\tilde{u}^{n+1}}{r^2}\right] \tag{17}$$

$$(18) \qquad\qquad \tilde{v}^{n+1} = \bar{v}^{n+1} - \Delta t Pr\left[\frac{1}{r}\left(r\frac{\partial\tilde{v}^{n+1}}{\partial r}\right) + \frac{\partial^2\tilde{v}^{n+1}}{\partial z^2}\right]$$

Step 3

The pressure terms are calculated from the Poisson equation using the intermediate velocities. This ensures that continuity is satisfied. The pressure values obtained are then used to calculate the corrected velocity values. The Poisson equation is expressed in the following way:

$$\nabla^2 p^{n+1} = \Delta t\left[\frac{1}{r}\frac{\partial}{\partial r}(r\tilde{u}^{n+1}) + \frac{\partial\tilde{u}^{n+1}}{\partial z}\right] \tag{19}$$

In the following equation, the corrected velocity values, u and v, are calculated using the pressure value solved from (21):

$$u^{n+1} = \tilde{u}^{n+1} - \Delta t\left(\frac{\partial p^{n+1}}{\partial r}\right) \tag{20}$$

$$v^{n+1} = \tilde{v}^{n+1} - \Delta t\left(\frac{\partial p^{n+1}}{\partial z}\right) \tag{21}$$

Step 4

Once the corrected velocities have been computed, the temperature at the next time step, T^{n+1}, can be calculated directly from the velocity field. The azimuthal velocity is also calculated at this step. There are no pressure terms in the θ momentum equation, so w can be calculated the same way as the temperature. Both are solved with the same procedure used to solve the u and v velocities. In the case of the energy equation, the convective terms are advanced in time using the Adams–Bashforth method,

$$\bar{T}^{n+1} = T^n - \Delta t\left[\frac{3}{2}\left(u^n\frac{\partial T^n}{\partial r}\right) - \frac{1}{2}\left(u^{n-1}\frac{\partial T^{n-1}}{\partial r}\right)\right] - \Delta t\left[\frac{3}{2}\left(v^n\frac{\partial T^n}{\partial z}\right) - \frac{1}{2}\left(v^{n-1}\frac{\partial T^{n-1}}{\partial z}\right)\right] \tag{22}$$

while the diffusive terms are solved using the implicit Euler scheme:

$$T^{n+1} = \bar{T}^{n+1} - \Delta t\left[\frac{1}{r}\frac{\partial}{\partial r}\left(r\frac{\partial T^{n+1}}{\partial r}\right) + \frac{\partial^2 T^{n+1}}{\partial z^2}\right] \tag{23}$$

This same procedure is then applied to calculate the azimuthal velocity, w.

$$\bar{w}^{n+1} = w^n - \Delta t\left[\frac{3}{2}\left(u^n\frac{\partial w^n}{\partial r}\right) - \frac{1}{2}\left(u^{n-1}\frac{\partial w^{n-1}}{\partial r}\right)\right] - \Delta t\left[\frac{3}{2}\left(v^n\frac{\partial w^n}{\partial z}\right) - \frac{1}{2}\left(v^{n-1}\frac{\partial w^{n-1}}{\partial z}\right)\right]$$

$$- \Delta t\left[\frac{3}{2}\left(\frac{u^n w^n}{r}\right) - \frac{1}{2}\left(\frac{u^{n-1}w^{n-1}}{r}\right)\right] \tag{24}$$

$$w^{n+1} = \bar{w}^{n+1} - \Delta t\left[\frac{1}{r}\frac{\partial}{\partial r}\left(r\frac{\partial w^{n+1}}{\partial r}\right) + \frac{\partial^2 w^{n+1}}{\partial z^2}\right] + \Delta t\frac{w^{n+1}}{r^2} \tag{25}$$

Spatial discretization

The spatial variables are discretized by dividing the domain Ω into non-overlapping, four node isoparametric finite elements. To apply the finite element method, the equations are first written in the integral form. Since an approximate solution is assumed, the governing differential equations are equal to a residual other than zero. Using the Galerkin method of the weighted residuals, these integrals are multiplied by a weighting function and forced to equal zero. The resulting form of the equations is called the weak form. The bilinear quadrilateral interpolation functions chosen are shown below in natural coordinates:

$$\Phi_1 = \tfrac{1}{4}(1-r)(1-s) \tag{26}$$

$$\Phi_2 = \tfrac{1}{4}(1+r)(1-s) \tag{27}$$

$$\Phi_3 = \tfrac{1}{4}(1-r)(1+s) \tag{28}$$

$$\Phi_4 = \tfrac{1}{4}(1+r)(1+s) \tag{29}$$

The approximate solution for each of the variables can now be written as:

$$u = u_\alpha \Phi_\alpha \tag{30}$$

$$v = v_\alpha \Phi_\alpha \tag{31}$$

$$w = w_\alpha \Phi_\alpha \tag{32}$$

$$p = p_\alpha \Phi_\alpha \tag{33}$$

$$T = T_\alpha \Phi_\alpha \tag{34}$$

where u_α, v_α, w_α, p_α, and T_α are the discretized variables at the node αth node. These variables are later assembled into a global matrix, and the global form of these variables will be denoted as U, V, W, P and T. After applying the divergence theorem in conjunction with the boundary conditions, the original set of partial differential equations now become the assembled system of equations in the following form:

$$\left(M_{\alpha\beta} + \Delta t Pr S_{\alpha\beta} + \frac{\Delta t}{r} Pr M_{\alpha\beta 2} \right) U_\beta^{n+1} = M_{\alpha\beta} U_\beta^n - \Delta t K_{\alpha\beta\gamma}^r U_\beta^n U_\gamma^n - \Delta t K_{\alpha\beta\gamma}^z V_\beta^n U_\gamma^n$$

$$+ \frac{\Delta t}{r} M_{\alpha\beta\gamma} W_\beta^n W_\gamma^n + \Delta t S_2 \tag{35}$$

$$(M_{\alpha\beta} + \Delta t Pr S_{\alpha\beta}) V_\beta^{n+1} = M_{\alpha\beta} V_\beta^{n+1} - \Delta t K_{\alpha\beta\gamma}^r U_\beta^n V_\gamma^n - \Delta t K_{\alpha\beta\gamma}^z V_\beta^n V_\gamma^n + \Delta t S_1 \tag{36}$$

$$\left(M_{\alpha\beta} + \Delta t Pr S_{\alpha\beta} + \frac{\Delta t}{r^2} Pr M_{\alpha\beta} \right) W_\beta^{n+1} = M_{\alpha\beta} W_\beta^n - \Delta t K_{\alpha\beta\gamma}^r U_\beta^n W_\gamma^n$$

$$- \Delta t K_{\alpha\beta\gamma}^z V_\beta^n W_\gamma^n - \frac{\Delta t}{r} M_{\alpha\beta\gamma} U_\beta^n W_\gamma^n \tag{37}$$

$$(M_{\alpha\beta} + \Delta t Pr S_{\alpha\beta}) T_\beta^{n+1} = M_{\alpha\beta} T_\beta^{n+1} - \Delta t K_{\alpha\beta\gamma}^r U_\beta^n T_\gamma^n - \Delta t K_{\alpha\beta\gamma}^z V_\beta^n T_\gamma^n \tag{38}$$

The Poisson equation can be written as:

$$S_{\alpha\beta} P_\beta^{n+1} = -\Delta t (D_{\alpha\beta}^r U_\beta^{n+1} + D_{\alpha\beta}^z V_\beta^{n+1} + M_{\alpha\beta} U_\beta^{n+1}) \tag{39}$$

Finally, the corrected velocity values are solved using the following equations:

$$M_{\alpha\beta} U_\beta^{n+1} = M_{\alpha\beta} \tilde{U}_\beta^{n+1} - \Delta t D_{\alpha\beta}^r P_\beta^{n+1} \tag{40}$$

$$M_{\alpha\beta} V_\beta^{n+1} = M_{\alpha\beta} \tilde{V}_\beta^{n+1} - \Delta t D_{\alpha\beta}^z P_\beta^{n+1} \tag{41}$$

The coefficient matrices from the above finite element equations are defined as follows:

$$M_{\alpha\beta} = \int_\Omega (\Phi_\alpha \Phi_\beta) \, d\Omega \tag{42}$$

$$M_{\alpha\beta 2} = \int_\Omega \frac{1}{r} (\Phi_\alpha \Phi_\beta) \, d\Omega \tag{43}$$

$$S_{\alpha\beta} = \int_\Omega (\Phi_{\alpha,r} \Phi_{\beta,r}) \, d\Omega + \int_\Omega (\Phi_{\alpha,z} \Phi_{\beta,z}) \, d\Omega \tag{44}$$

$$K_{\alpha\beta\gamma}^r = \int_\Omega (\Phi_\alpha \Phi_\beta \Phi_{\gamma,r}) \, d\Omega \tag{45}$$

$$K_{\alpha\beta\gamma}^z = \int_\Omega (\Phi_\alpha \Phi_\beta \Phi_{\gamma,z}) \, d\Omega \tag{46}$$

$$D_{\alpha\beta}^r = \int_\Omega (\Phi_\alpha \Phi_{\beta,r})\, d\Omega \tag{47}$$

$$D_{\alpha\beta}^z = \int_\Omega (\Phi_\alpha \Phi_{\beta,z})\, d\Omega \tag{48}$$

The coefficients M, S, K and D represent the mass matrix, diffusion matrix, convection matrix, and the transpose of the divergence matrix respectively. In the axisymmetric case, $d\Omega$ is simply $2\pi r$. Part of the results are plotted in the form of streamlines, and the stream function is defined as:

$$\nabla^2 \psi = r\omega \tag{49}$$

where

$$\nabla^2 \psi = \frac{\partial^2 \psi}{\partial r^2} - \frac{1}{r}\frac{\partial \psi}{\partial r} + \frac{\partial^2 \psi}{\partial z^2} \tag{50}$$

and

$$\omega = \frac{\partial u}{\partial z} - \frac{\partial v}{\partial r} \tag{51}$$

The stream function equation is also discretized using finite elements. After multiplying by the weighting function in the weak formulation, the following equation is derived.

$$S_{\alpha\beta}\psi_\beta = r(D_{\alpha\beta}^r V - D_{\alpha\beta}^z U) \tag{52}$$

RESULTS AND DISCUSSION

Two cases are investigated, one dealing with the rectangular cavity, and the other dealing with the cylindrical cavity for the axisymmetric flow analysis. The mesh configurations are shown in *Figure 2* and *Figure 18*. The aspect ratios of the rectangular cavity and the cylindrical cavity studied are both 0.5. The Rayleigh number is chosen to be 1.771×10^5, and the Prandtl number is 0.007. For the rectangular cavity, two different mesh configurations are used for each case, one for the vertical baffle, and one for the horizontal baffle. For each baffle configuration, eight different jitter frequencies are tested, four in the vertical direction and four in the horizontal direction. The results show the streamline pattern and temperature contour plotted from the time averaged values computed for each case. For the cylindrical cavity, only the horizontal baffle is tested. The results for this case show plots of the velocity vector, streamline pattern, and temperature contour. For both cases, the figures described also display the forcing function, S_1 or S_2, velocity, and temperature point data traced over time at two points, one in the lower left corner of the cavity, and one near the baffle, both chosen arbitrarily. When the results were obtained, we hoped to see as little disturbance to the flow as possible. This means having a symmetric streamline pattern, a conductive temperature contour, and synchronous point data response at low amplitudes of oscillations.

Summary of rectangular cavity flow without baffles

In the first case of this study, a semi-implicit finite element scheme is used to solve the rectangular heated cavity flow problem with the addition of baffles under different frequencies and directions of gravity modulation. No benchmark cases are used to test the numerical code for the rectangular cavity problem since it has already been tested and presented in previously published literature[3]. These published results are used as a reference for comparison with the results containing the baffle. This section summarizes the results obtained for the rectangular
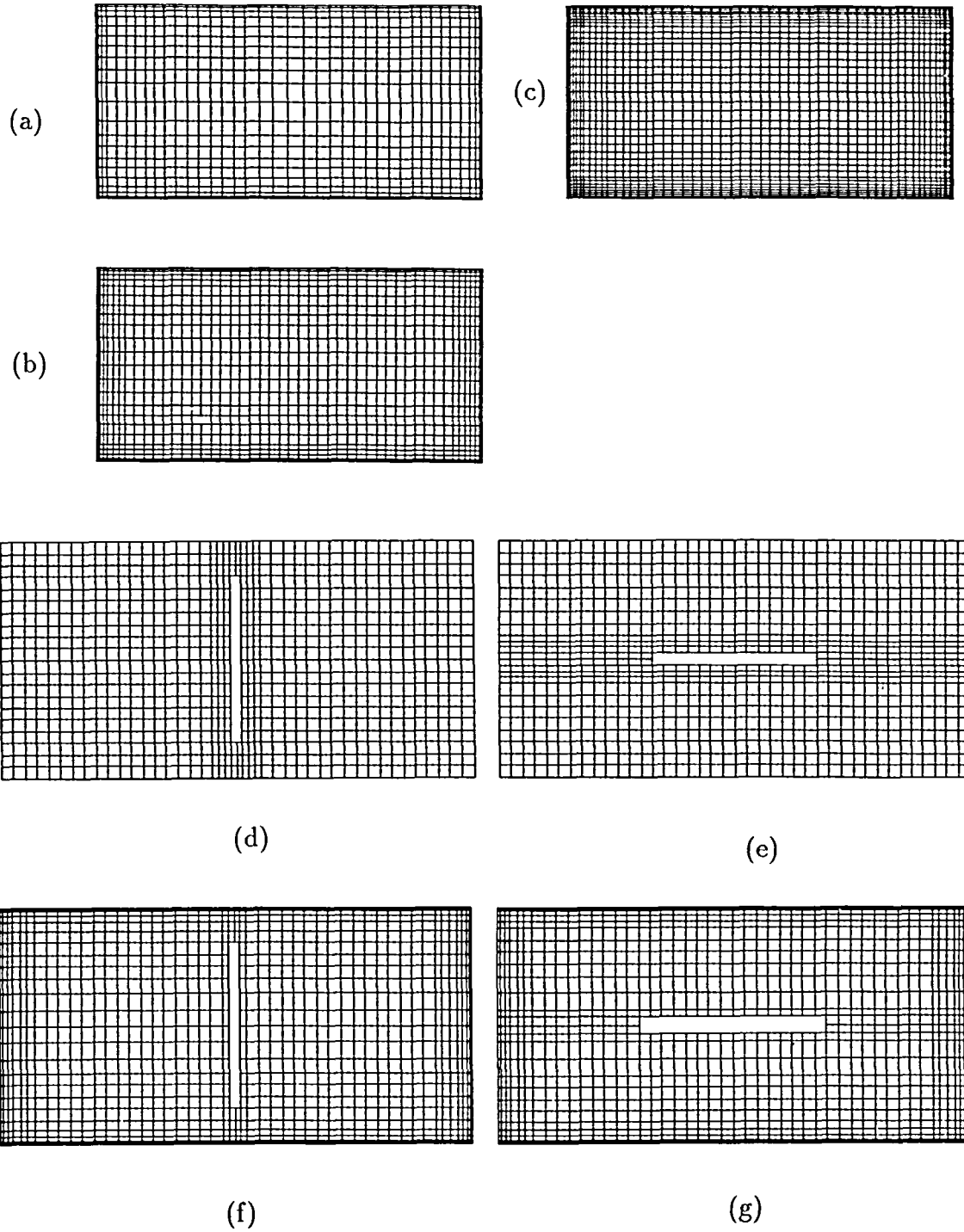
(a)

(c)

(b)

(d)

(e)

(f)

(g)

Figure 2   Mesh configuration: (a) non-uniform mesh (20 × 38); (b) non-uniform mesh (24 × 48); (c) non-uniform mesh (38 × 56); (d) & (e) non-uniform mesh with baffles for natural convection; (f) & (g) non-uniform mesh with baffles for natural convection with thermocapillary effects

Table 1 Influence of finite element mesh on the solution

Mesh	$\omega = 45.5, Ma = -100$ zero-g (vertical jitter)			$\omega = 200, Ma = -100$ zero-g (horizontal jitter)		
	Nu_h	Nu_c	Max$|\Psi|$	Nu_h	Nu_c	Max$|\Psi|$
20 × 38	1.998	2.008	0.222	2.051	2.055	0.634
24 × 48	2.001	2.004	0.220	2.063	2.066	0.684
38 × 56	2.002	2.004	0.220	2.067	2.068	0.700

cavity flow analysis when no baffles are used. The modulation of gravity has a stabilizing effect on the flow by suppressing convection until a certain critical frequency is reached. The vertical jitter frequencies tested are 4543, 200, 45.5, and 20; the horizontal jitter frequencies tested are 450, 200, 85, and 40. When the jitter is acting in the vertical direction, one would see symmetrical streamline patterns at all jitter frequencies. The temperature contours displays conductive flow until a frequency of 20 is reached. At $\omega = 20$, convection sets in. When a horizontal jitter is applied on the flow, convection begins to set in at a frequency of 200. In addition, the point data respond in a synchronous manner until $\omega = 85$ is reached, after which the response becomes random. The streamline pattern loses its symmetry at a jitter frequency of 40.

In the second part of the study, thermocapillary effects are included in the analysis. Two Marangoni numbers are used, 100 and 1000. A grid independence study for three different meshes as shown in *Figure 2a–c* is listed in *Table 1*. Because of the computational cost and accuracy considerations, by observing *Table 1*, a 24 × 48 non-uniform mesh is used in this paper to provide fine grid spacing near the boundaries of the cavity. When the Marangoni number of 100 is used, the streamline patterns are unsymmetrical, and for the most part, the circulation takes place near the free surface. Furthermore, weak convective motion can be detected near the free surface. When a vertical frequency of 20 is reached, the flow regime becomes dominated by strong natural convection. The point data are synchronous, but turns subharmonic at a vertical frequency of 20. Similar results are found for the horizontal jitter cases. However, at the lowest jitter frequency of 85, the point data are random instead of being subharmonic. When the higher Marangoni is used in the computations, the flow regimes at the lowest frequencies are found to be dominated by natural convection under both vertical and horizontal gravity modulation. In addition, the horizontal jitter has a more stabilizing effect on the temperature point data, changing its response from random to periodic.

Natural convection in rectangular cavity flow with baffles

The results for the cases with baffles are shown in *Figures 3 to 17*. In the first part of case 1, natural convection is the only driving mechanism considered. At the higher frequencies, no significant differences can be found in the time averaged plots or the point data for the addition of a baffle. More differences can be detected at the lower frequencies. Only the more significant cases are summarized here. *Figure 3* shows the case for the vertical placement of the baffle under a vertical jitter frequency of 45.5, and the flow behaves as expected in this case. However, when the vertical jitter frequency decreases to 20, the results in *Figure 4* show that use of the vertical baffle is able to decrease the amplitude of temperature oscillations. The vertical baffle produced better results under horizontal gravity modulation. For example, *Figure 5* shows the case for the vertical placement of the baffle under a horizontal jitter frequency of 200. At this frequency, if no baffles are used, convection would begin to set in. However, with the baffle, the isotherms show that convection is suppressed. Another example is shown in *Figure 6*. In this example, the vertical baffle used for $\omega = 85$ shows an improvement in point data response. Instead of the high frequency, random velocity point data behaviour one would expect when no baffles are
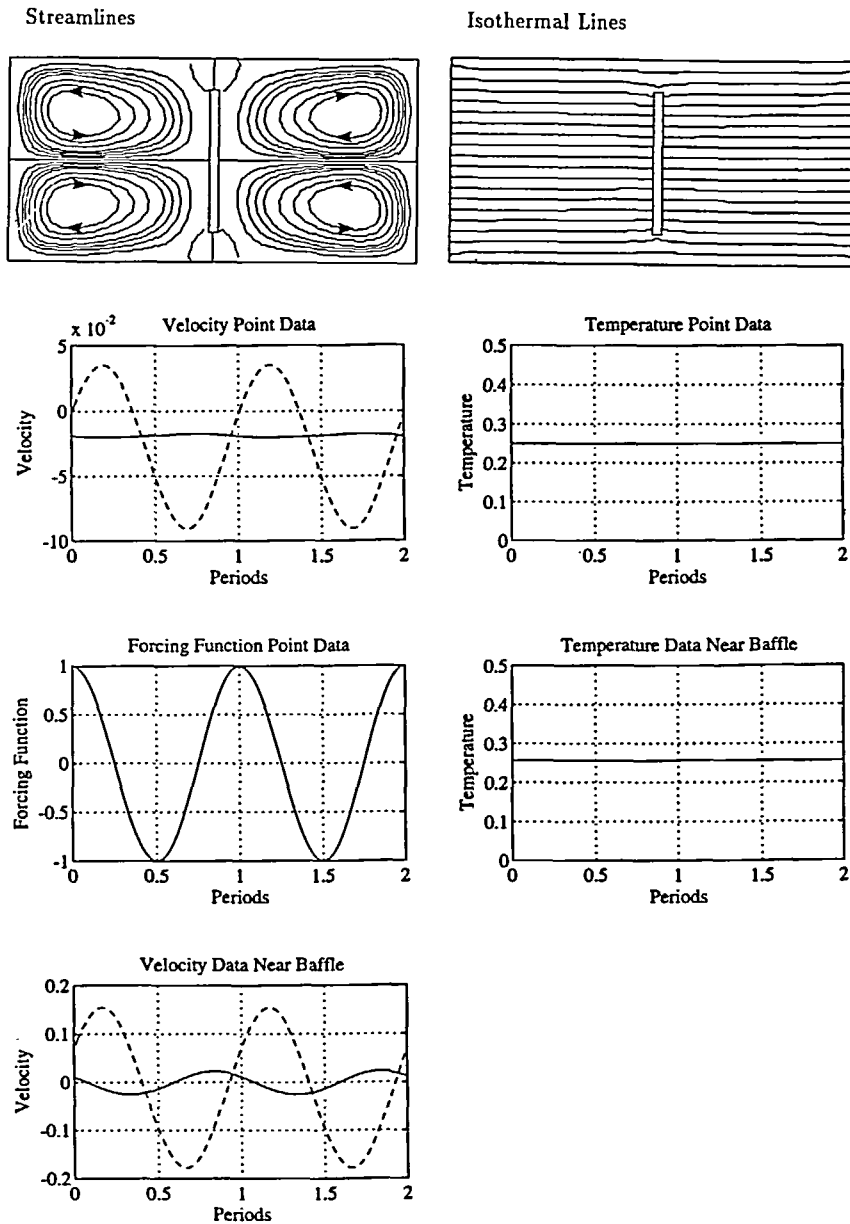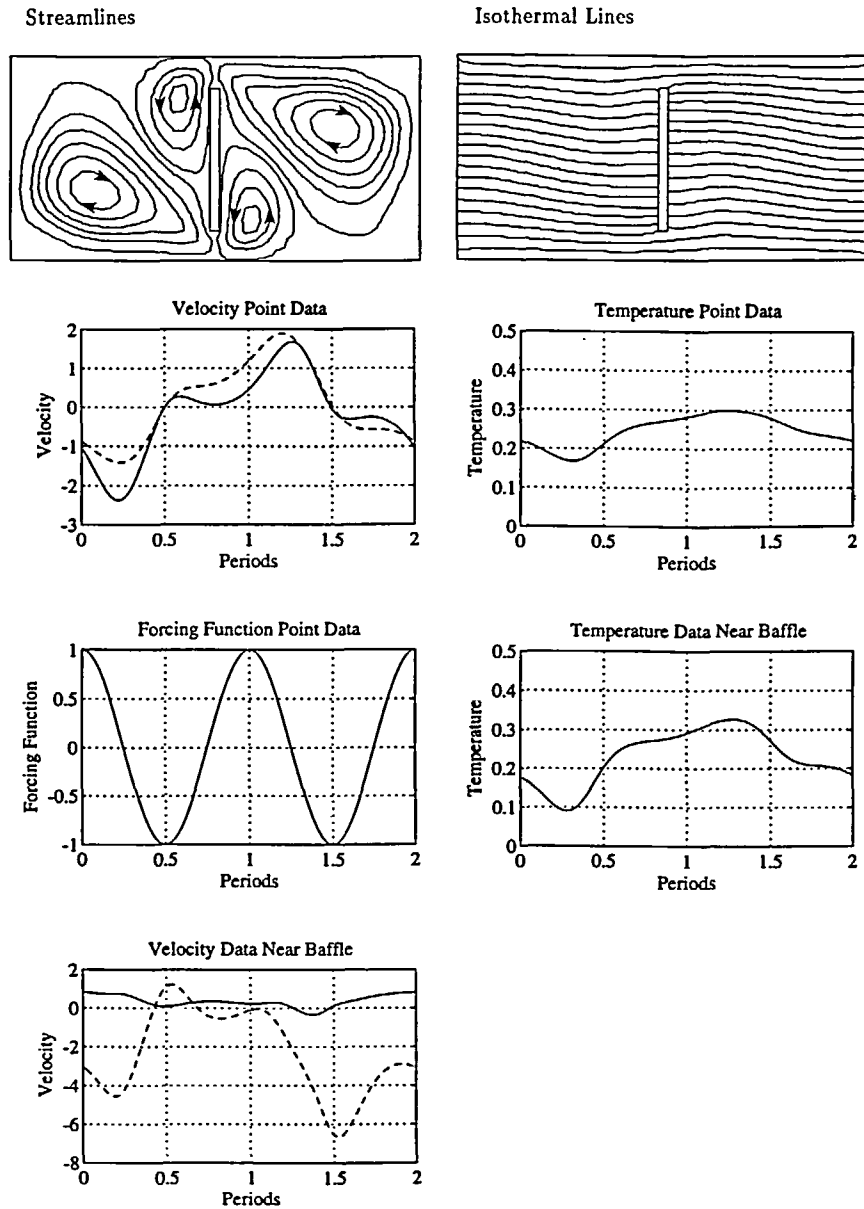
Streamlines   Isothermal Lines

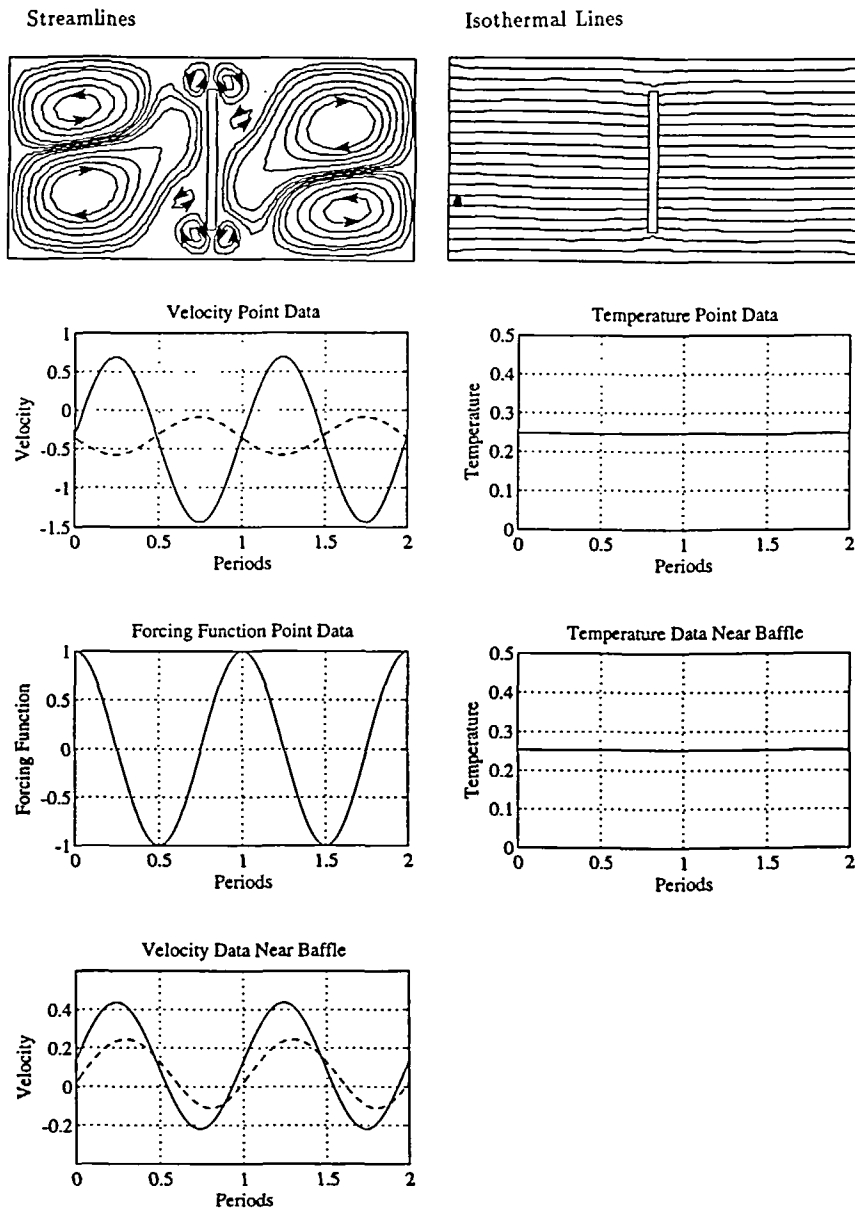*Figure 3* Time-averaged results for $Ra = 1.771 \times 10^5$, $Pr = 0.007$, $\eta = 1.0$, $\omega = 45.5$, $Ar = 0.5$, zero-g, vertical baffle (vertical jitter). ($\psi_{max} = 0.01395$, $\psi_{min} = -0.01395$)

used, the results show synchronous response from the velocity point data. The last example is shown in *Figure 7*, the point data in this Figure show some improvement which resulted from the presence of the vertical baffle at the horizontal jitter frequency of 40. With the addition of the vertical baffle, the point data response is subharmonic instead of random, and the temperature oscillates at a smaller amplitude than the case without the baffle.

Streamlines   Isothermal Lines

Velocity Point Data

Temperature Point Data

Forcing Function Point Data

Temperature Data Near Baffle

Velocity Data Near Baffle

Figure 4   Time-averaged results for $Ra = 1.771 \times 10^5$, $Pr = 0.007$, $\eta = 1.0$, $\omega = 20$, $Ar = 0.5$, zero-g, vertical baffle (vertical jitter). ($\psi_{max} = 0.3427$, $\psi_{min} = -0.3352$)

The same analysis is now done for the cases where the horizontal baffle is used. At a vertical jitter frequency of 45.5, shown in *Figure 8*, the results obtained show no significant deviation from the cases without the baffle. The main improvement is the suppression of convection at the low vertical jitter frequency of 20. The isotherms found in *Figure 9* shows that, at this frequency, the flow remains in the conduction regime. In addition, the point data at this frequency

Streamlines   Isothermal Lines

Velocity Point Data   Temperature Point Data

Forcing Function Point Data   Temperature Data Near Baffle
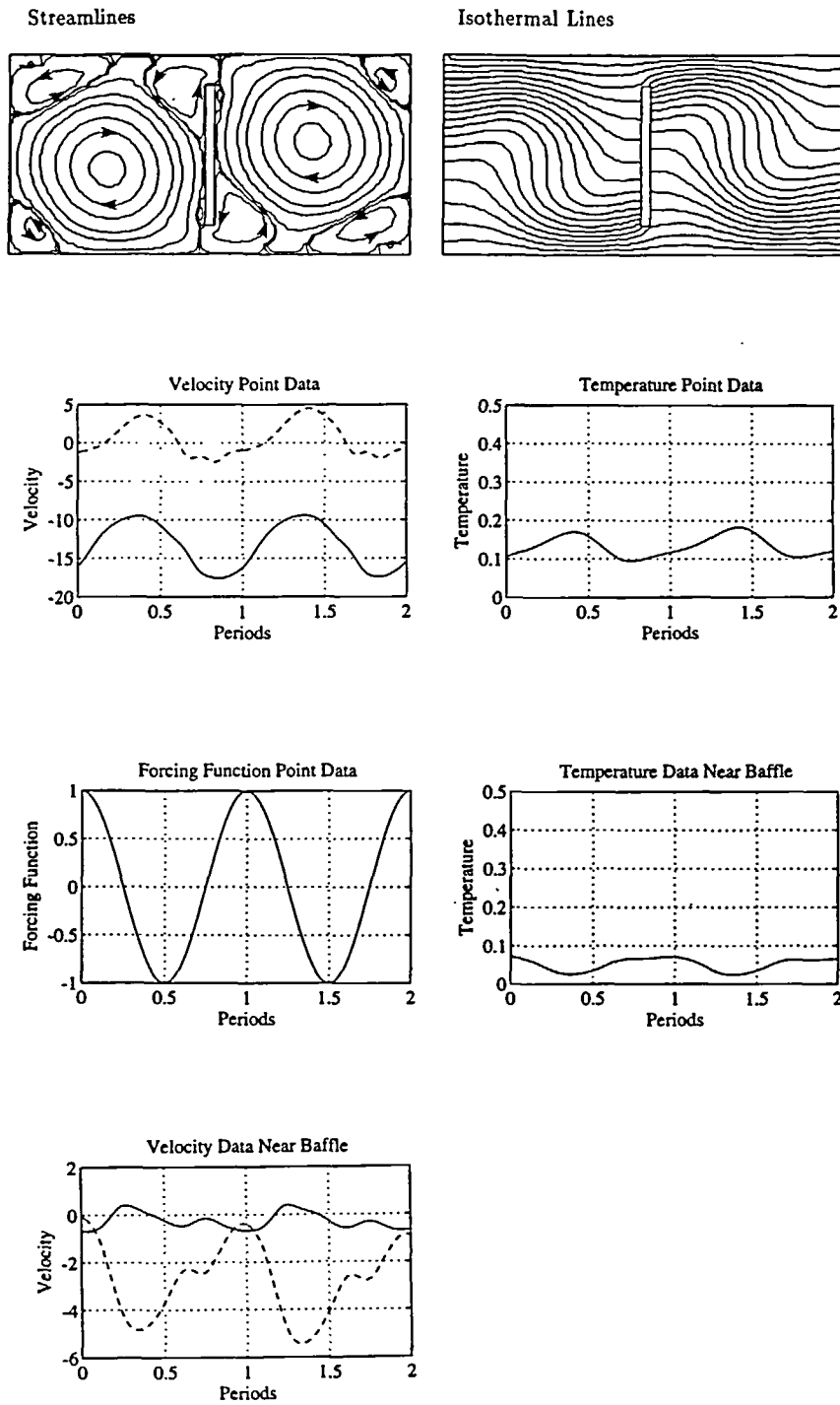
Velocity Data Near Baffle

Figure 5   Time-averaged results for $Ra = 1.771 \times 10^5$, $Pr = 0.007$, $\eta = 1.0$, $\omega = 200$, $Ar = 0.5$, zero-g, vertical baffle (horizontal jitter). ($\psi_{max} = 0.1345$, $\psi_{min} = -0.1345$)

show synchronous response with a decreased amplitude of oscillation compared to the corresponding case without the baffle. In fact, when no baffles are used, convection dominates the flow, and the point data response is subharmonic. At a horizontal frequency of 85, shown in *Figure 10*, the use of the horizontal baffle results in a significant decrease in the maximum stream function, and the point data are found to be synchronous near the baffle only. Finally,

Streamlines   Isothermal Lines
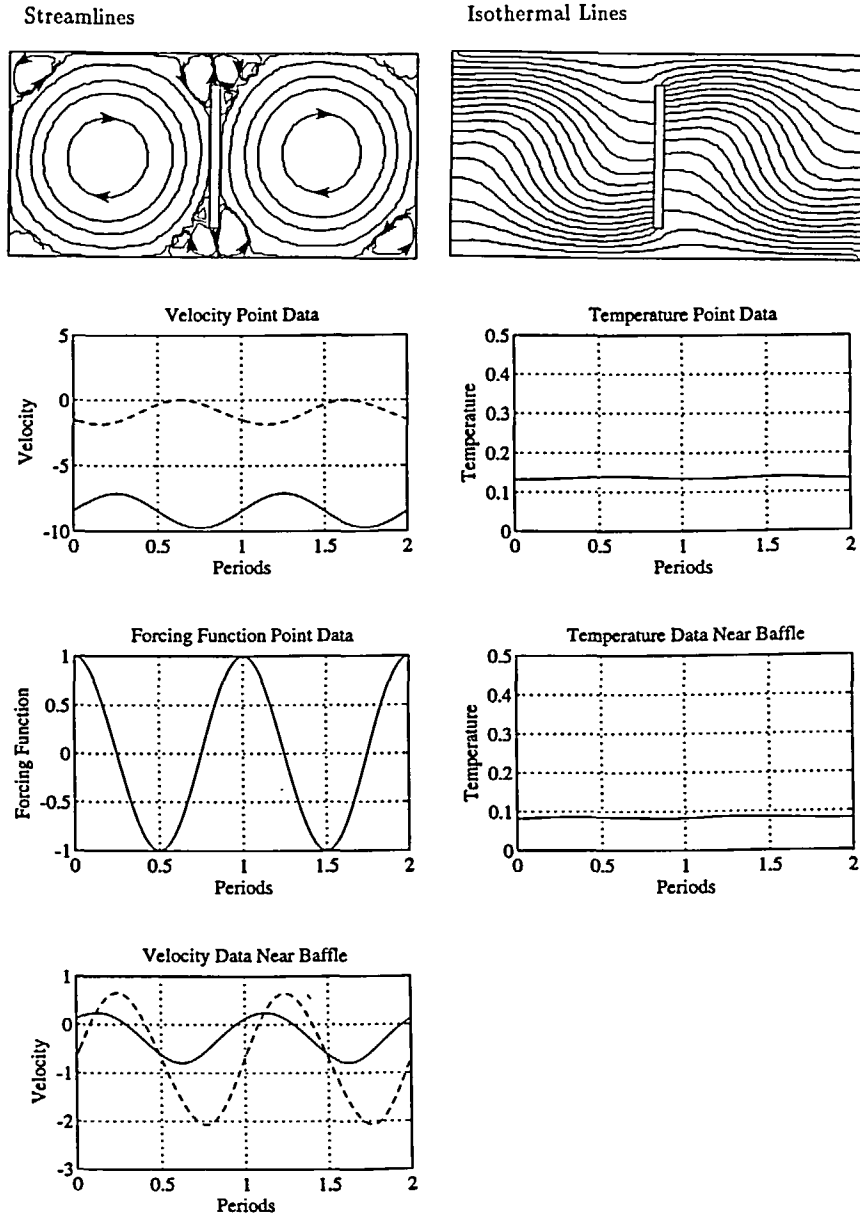
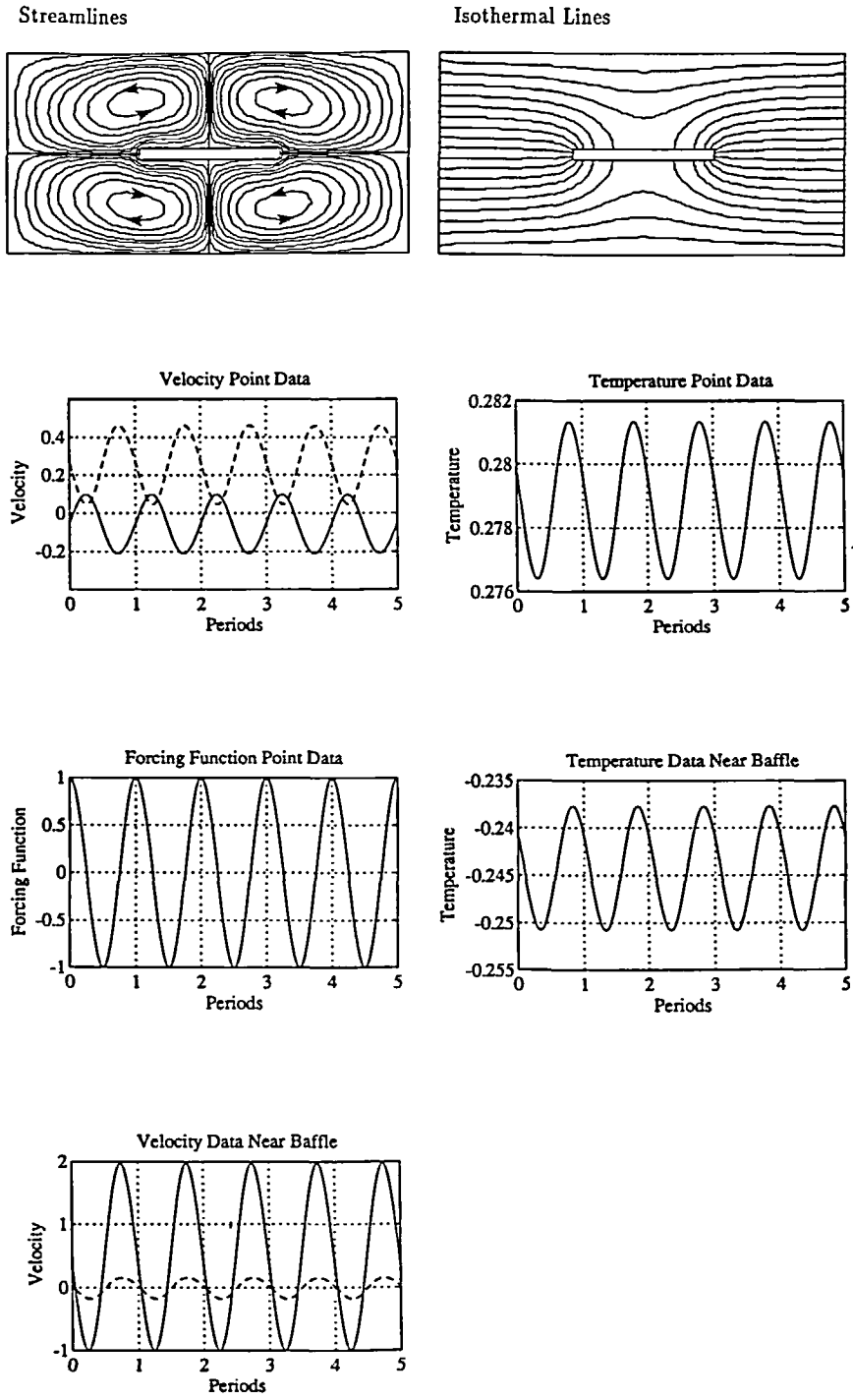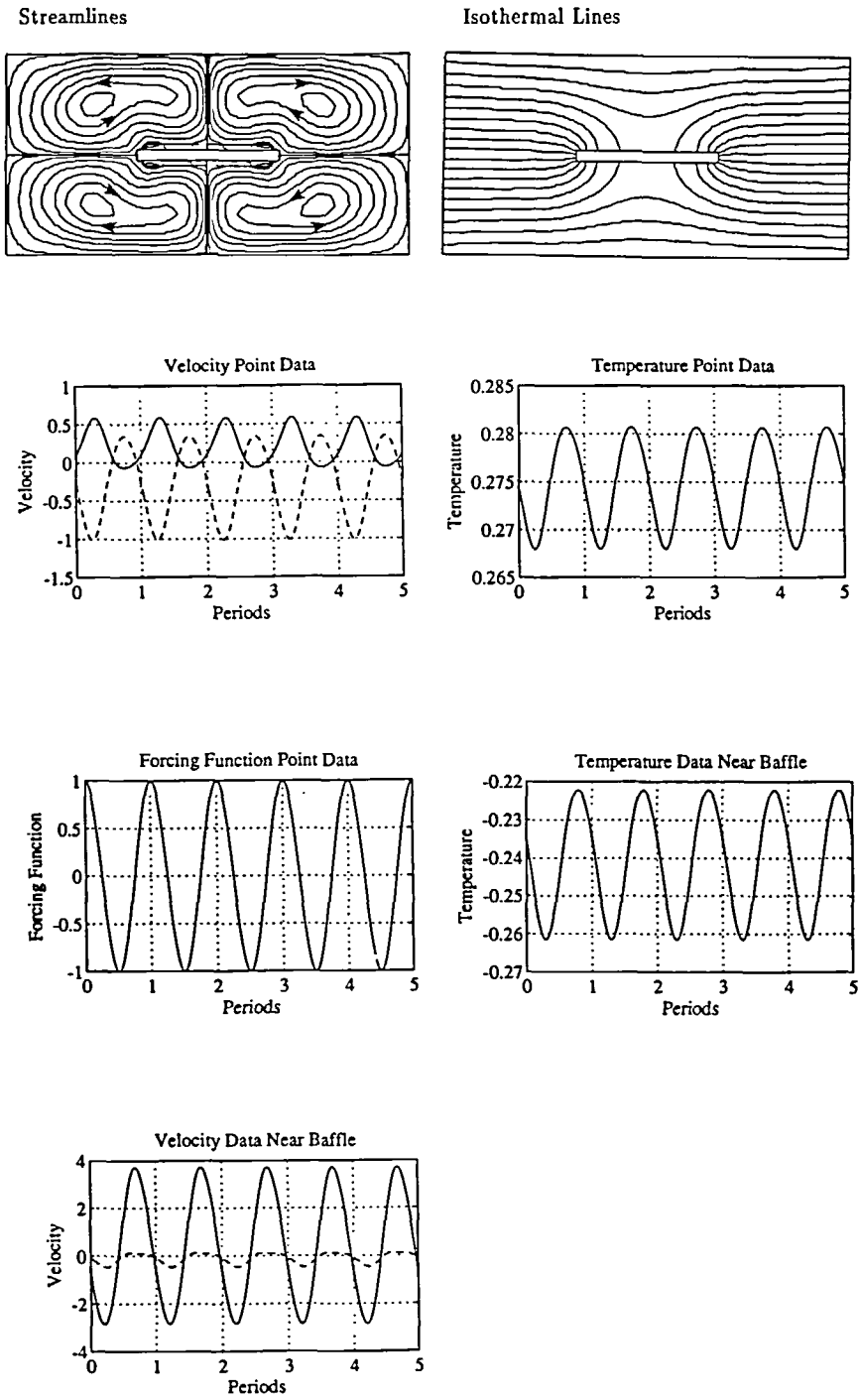*Figure 6* Time-averaged results for $Ra = 1.771 \times 10^5$, $Pr = 0.007$, $\eta = 1.0$, $\omega = 85$, $Ar = 0.5$, zero-g, vertical baffle (horizontal jitter). ($\psi_{max} = 2.975$, $\psi_{min} = -2.975$)

at a horizontal jitter of 40, the oscillations are at a high amplitude, but also at a higher frequency than the flow without the baffle. The higher frequency, lower amplitude oscillations are significant improvements on the flow, because the higher the frequency, the less time exists for the growing crystal to actually be affected. This can be seen in *Figure 11*.
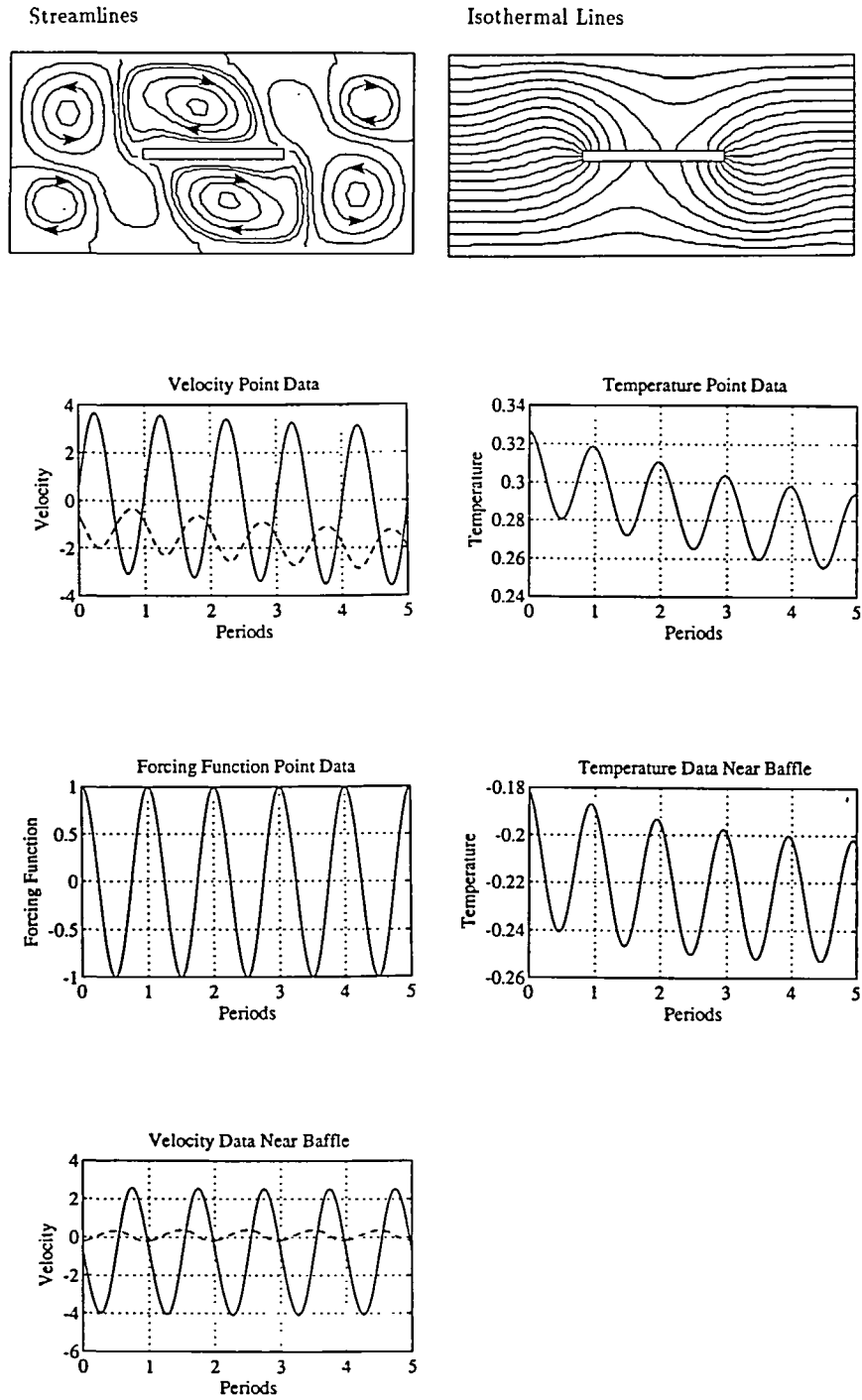
Figure 7 Time-averaged results for $Ra = 1.771 \times 10^5$, $Pr = 0.007$, $\eta = 1.0$, $\omega = 40$, $Ar = 0.5$, zero-g, vertical baffle (horizontal jitter). ($\psi_{max} = 4.335$, $\psi_{min} = -4.335$)

Streamlines   Isothermal Lines

Figure 8 Time-averaged results for $Ra = 1.771 \times 10^5$, $Pr = 0.007$, $\eta = 1.0$, $\omega = 45.5$, $Ar = 0.5$, zero-g, horizontal baffle (vertical jitter). ($\psi_{max} = 0.1182$, $\psi_{min} = -0.1182$)

Streamlines   Isothermal Lines

Figure 9   Time-averaged results for $Ra = 1.771 \times 10^5$, $Pr = 0.007$, $\eta = 1.0$, $\omega = 20$, $Ar = 0.5$, zero-g, horizontal baffle (vertical jitter). ($\psi_{max} = 0.1992$, $\psi_{min} = -0.1992$)

Streamlines   Isothermal Lines

Velocity Point Data

Temperature Point Data

Forcing Function Point Data

Temperature Data Near Baffle

Velocity Data Near Baffle

Figure 10 Time-averaged results for $Ra = 1.771 \times 10^5$, $Pr = 0.007$, $\eta = 1.0$, $\omega = 85$, $Ar = 0.5$, zero-g, horizontal baffle (horizontal jitter). ($\psi_{max} = 0.697$, $\psi_{min} = -0.5223$)

Natural convection and thermocapillary effects in rectangular cavity flow

In the second part of case 1, buoyancy induced convection and thermocapillary convection are the primary influences on the flow. The cases computed for a Marangoni number of 100 are shown in *Figures 12* to *15*. *Figure 12* shows the case for the vertical baffle under a vertical jitter frequency of 20. The main difference between using the baffle and not using the baffle is the lower amplitude of temperature oscillation when the baffle is used. When horizontal modulation is applied to the gravity field, the vertical baffle is able to produce synchronous point data behaviour instead of random behaviour at $\omega = 85$, shown in *Figure 13*. The horizontal baffle under a vertical jitter frequency of 20 is shown in *Figure 14*. Thermocapillary convection is present, and the temperature response is synchronous and at a very low amplitude. Under a horizontal frequency of 85, use of the horizontal baffle also shows significant improvement in the point data behaviour, because they are synchronous instead of non-periodic. This can be seen in *Figure 15*.

At the higher Marangoni number of 1000, the flow characteristics are very similar between the case without the baffle and with the vertical baffle. The main difference appears in the streamline pattern. The presence of the vertical baffle impedes the spreading of the thermocapillary effects, so the flow is dominated by natural convection. When the horizontal baffle is placed in the cavity, the flow is dominated by surface tension, as can be expected from analysis of the previous case, where the Marangoni is 100. *Figure 16* shows that the vertical placement of the baffle has detrimental effects to the flow behaviour at a vertical jitter frequency of 20. In this case, the point data oscillate at high amplitudes and in a random fashion. However, as *Figure 17* shows, the horizontal baffle is able to maintain synchronous response under the same frequency.

From the results observed in the study, the differences and conclusions can be summed up as follows. For the natural convection case, the addition of baffles were not able to eliminate convection and temperature oscillations at all frequencies and directions of modulation. In general, the effects of baffles depended on the direction of the baffle placement with respect to the modulation direction as well as modulation frequency. For the case with the free surface flow, the main difference between the vertical baffle and the horizontal baffle is the flow regime. At the lowest frequency, the flow becomes dominated by buoyancy induced convection for the vertical baffle in both modulation directions, but the flow with the horizontal placement of the baffle remains dominated by a weak thermocapillary convection, again in both modulation directions. For all cases, neither baffle induced temperature oscillations.

Axisymmetric flow analysis

In the second part of this study, the axisymmetric model of the heated cavity with and without the baffle is investigated using the same numerical scheme. The boundary conditions are shown in *Figure 1b*. The two Reynolds numbers used in the boundary conditions have the same basic definition, and the only difference is that Re_c is a measure of the crucible rotation rate, and Re_s is a measure of the crystal rotation rate. Subsequently, the crucible is used in the calculation of Re_c, and the crystal radius is used in the calculation of Re_s. The cylinder is a simple model of the actual crucible in which a crystal would be grown. However, much of the real problem has been simplified. For example, the current model assumes that the free surface interface between the crystal and the melt is flat. In the real situation, the shape of the interface should be determined from the results and not assumed *a priori*. The type of model used here, in which convective motion is the main concern, is called 'Czochralski bulk flow'. The driving forces of the flow include buoyancy induced convection and forced convection from the crystal and crucible rotation, as well as from the modulation of the gravity field.

Some benchmark cases are computed to test the validity of the numerical code developed for the axisymmetric flow analysis. These cases are taken from the examples computed by Crochet
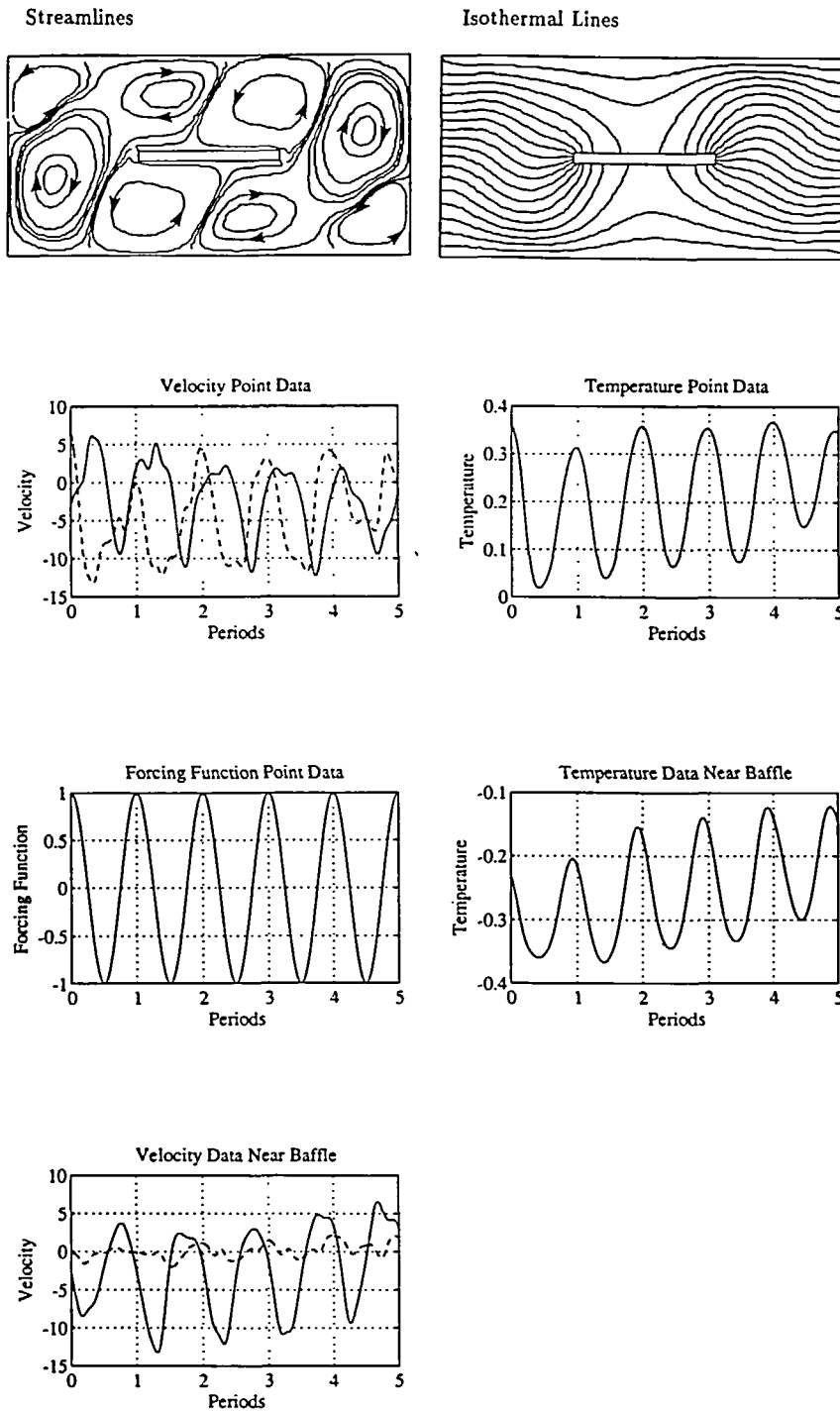
Streamlines   Isothermal Lines

Figure 11   Time-averaged results for $Ra = 1.771 \times 10^5$, $Pr = 0.007$, $\eta = 1.0$, $\omega = 40$, $Ar = 0.5$, zero-g, horizontal baffle (horizontal jitter). ($\psi_{max} = 1.2944$, $\psi_{min} = -1.2944$)
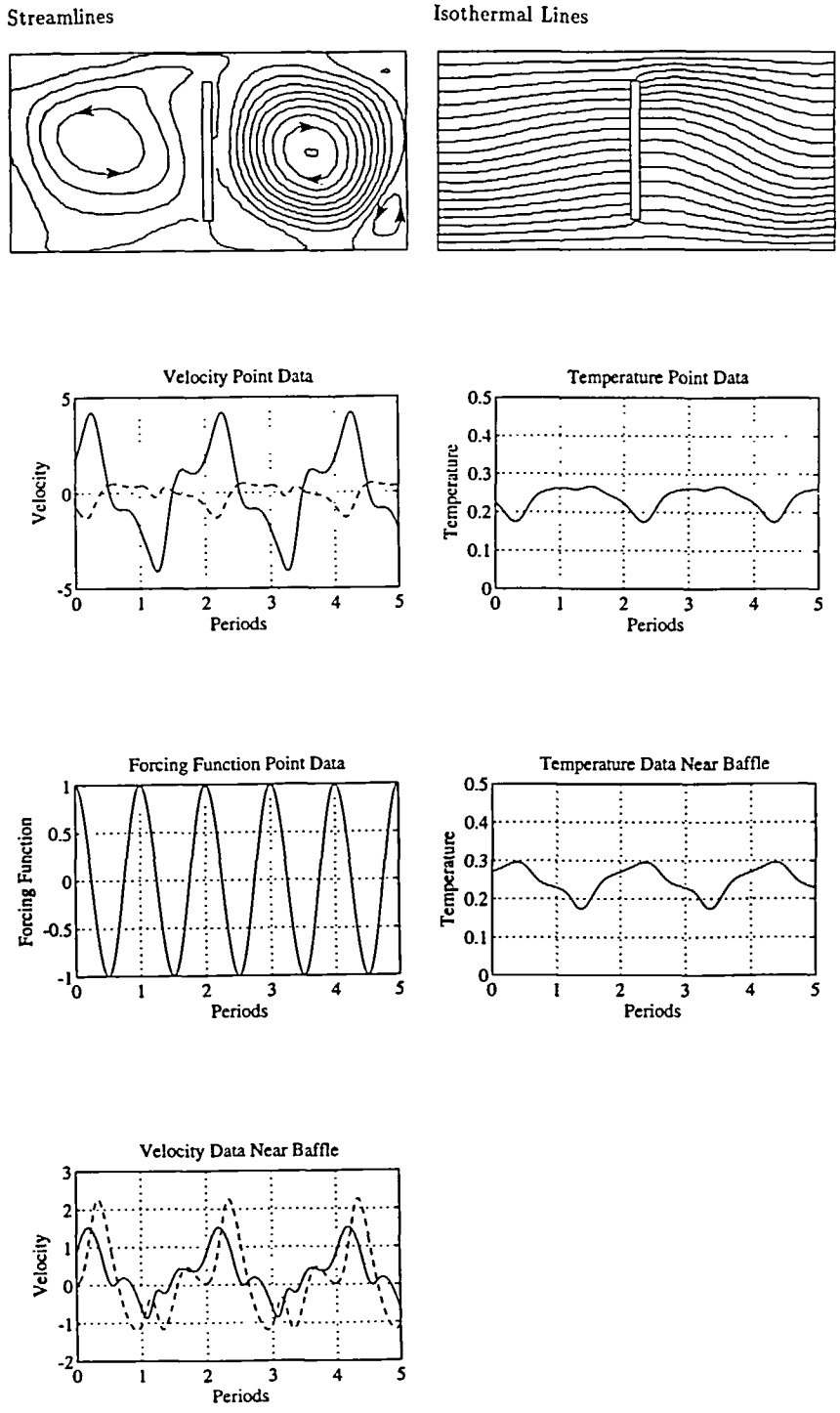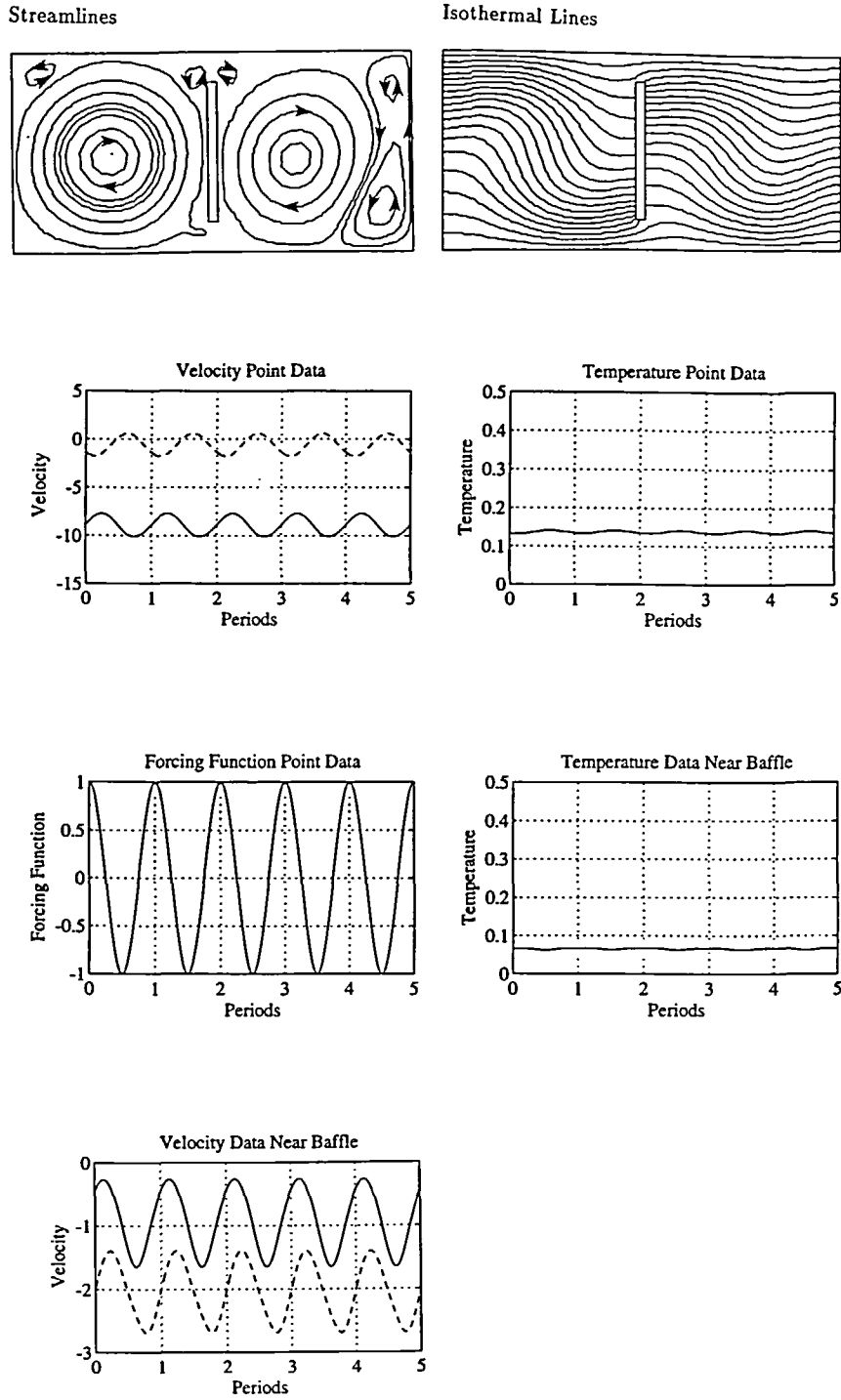
Streamlines

Isothermal Lines

Velocity Point Data

Temperature Point Data

Forcing Function Point Data

Temperature Data Near Baffle

Velocity Data Near Baffle

Figure 12   Time-averaged results for $Ra = 1.771 \times 10^5$, $Pr = 0.007$, $Ma = 100$, $\eta = 1.0$, $\omega = 20$, $Ar = 0.5$, zero-g, vertical baffle (vertical jitter). ($\psi_{max} = 0.9065$, $\psi_{min} = -0.9065$)

Streamlines

Isothermal Lines

Velocity Point Data

Temperature Point Data

Forcing Function Point Data

Temperature Data Near Baffle

Velocity Data Near Baffle

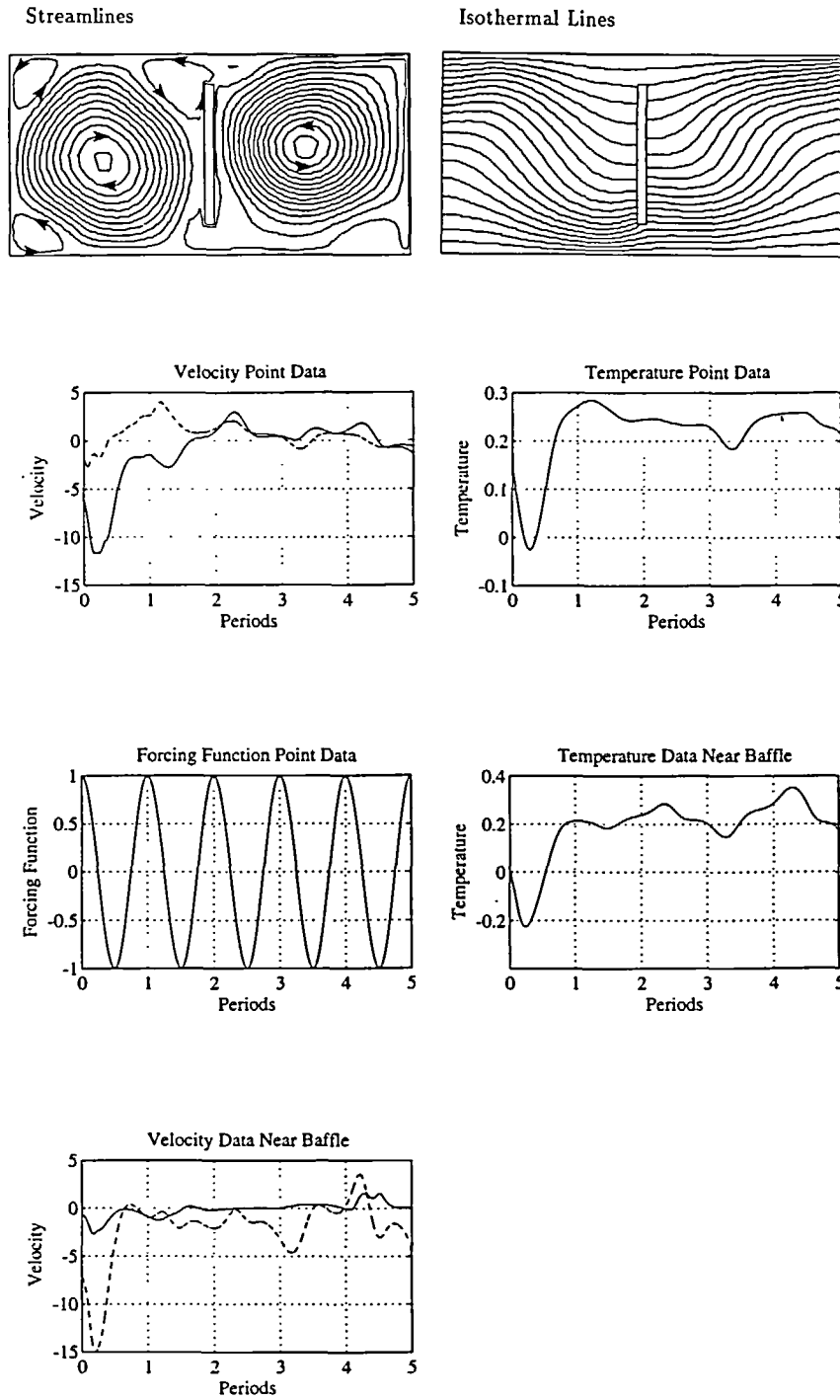*Figure 13* Time-averaged results for $Ra = 1.771 \times 10^5$, $Pr = 0.007$, $Ma = 100$, $\eta = 1.0$, $\omega = 85$, $Ar = 0.5$, zero-g, vertical baffle (horizontal jitter). ($\psi_{max} = 2.99$, $\psi_{min} = -2.99$)

Streamlines   Isothermal Lines
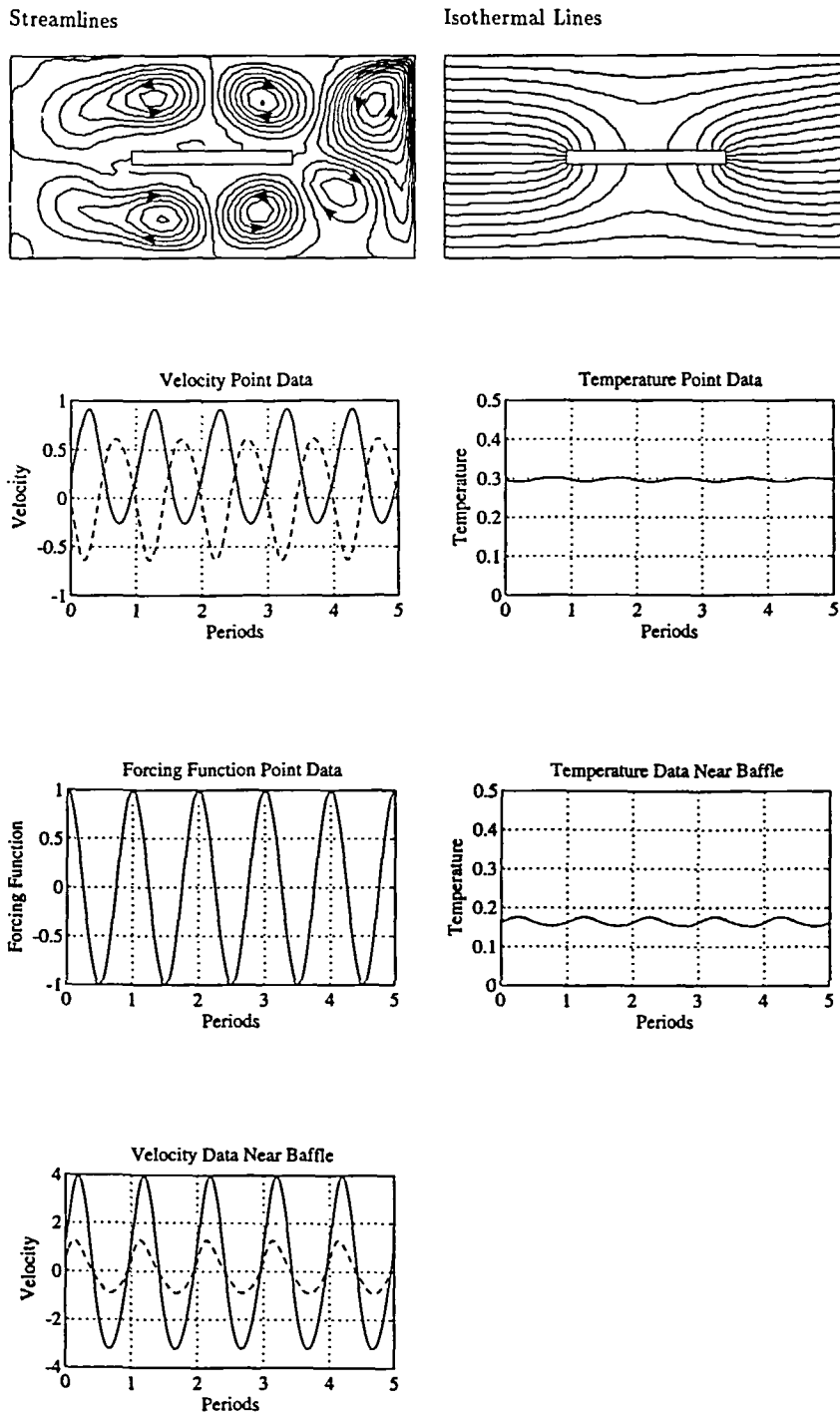
Figure 14   Time-averaged results for $Ra = 1.771 \times 10^5$, $Pr = 0.007$, $Ma = 100$, $\eta = 1.0$, $\omega = 20$, $Ar = 0.5$, zero-g, horizontal baffle (vertical jitter). ($\psi_{max} = 0.2563$, $\psi_{min} = -0.1905$)

Streamlines   Isothermal Lines
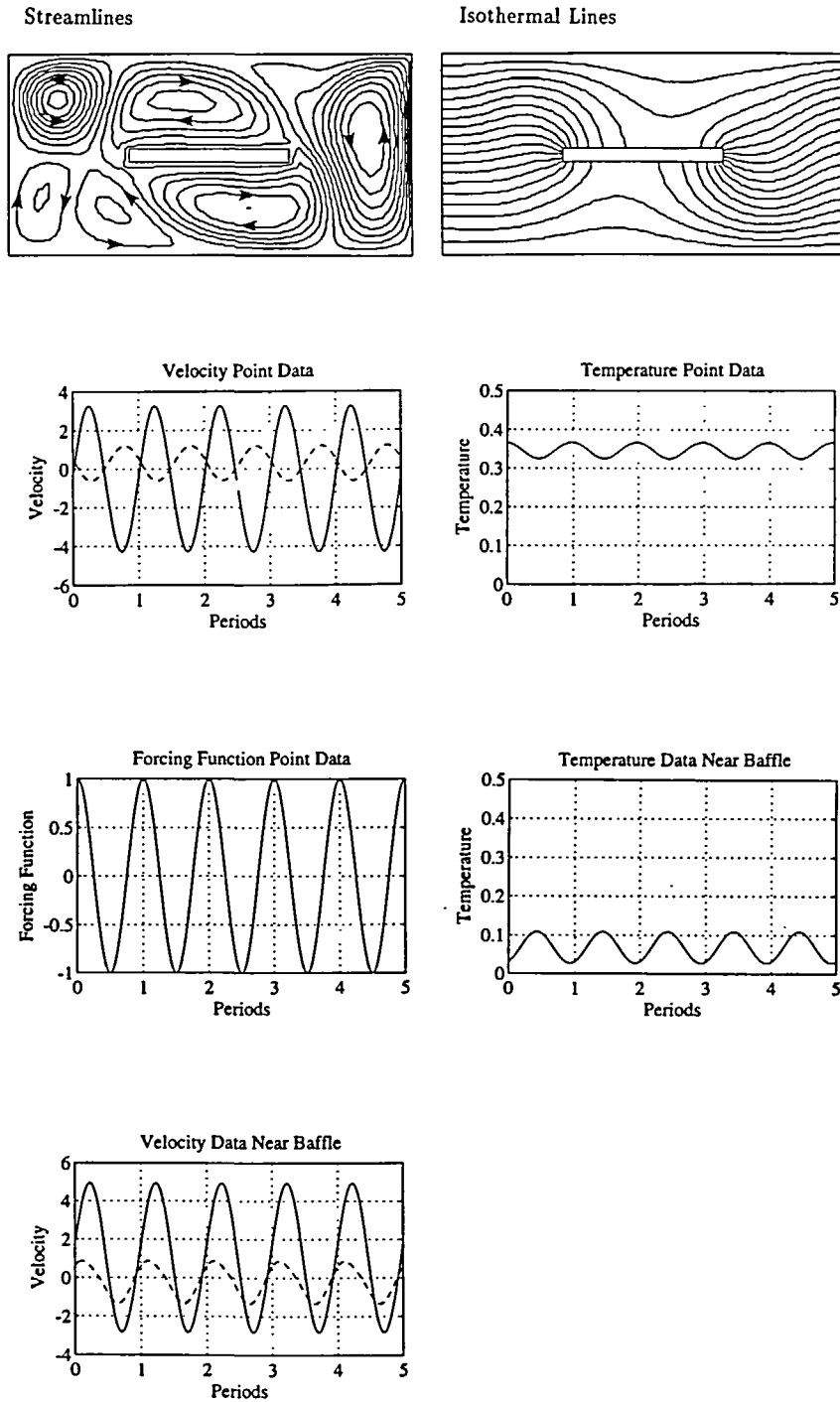
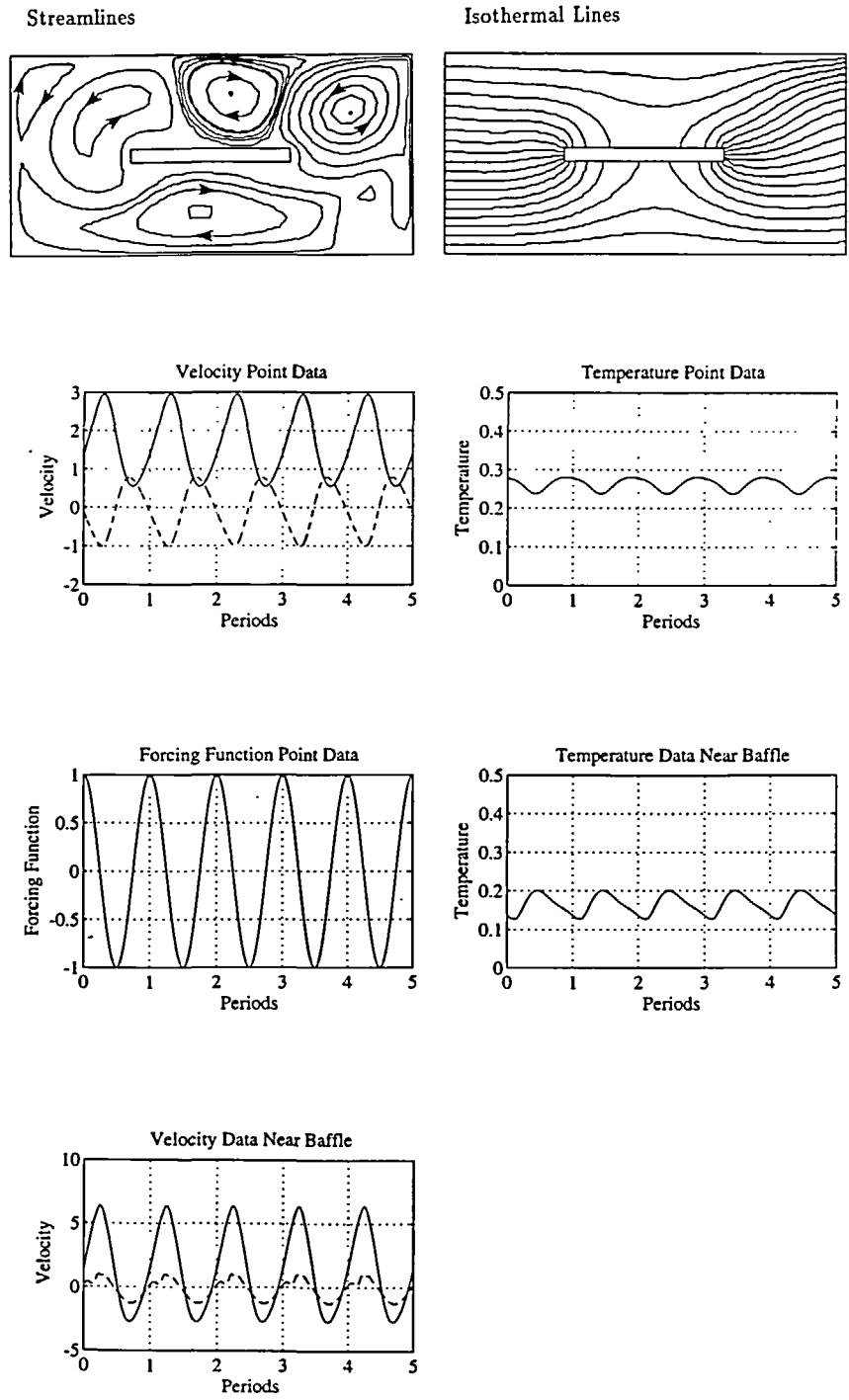*Figure 15* Time-averaged results for $Ra = 1.771 \times 10^5$, $Pr = 0.007$, $Ma = 100$, $\eta = 1.0$, $\omega = 85$, $Ar = 0.5$, zero-g, horizontal baffle (horizontal jitter). ($\psi_{max} = 0.6699$, $\psi_{min} = -0.427$)

Streamlines   Isothermal Lines

Figure 16   Time-averaged results for $Ra = 1.771 \times 10^5$, $Pr = 0.007$, $Ma = 1000$, $\eta = 1.0$, $\omega = 20$, $Ar = 0.5$, zero-g, vertical baffle (vertical jitter). ($\psi_{max} = 2.994$, $\psi_{min} = -2.4$)

Streamlines   Isothermal Lines

Velocity Point Data   Temperature Point Data

Forcing Function Point Data   Temperature Data Near Baffle

Velocity Data Near Baffle

Figure 17 Time-averaged results for $Ra = 1.771 \times 10^5$, $Pr = 0.007$, $Ma = 1000$, $\eta = 1.0$, $\omega = 20$, $Ar = 0.5$, zero-g, horizontal baffle (vertical jitter). ($\psi_{max} = 1.324$, $\psi_{min} = -0.7045$)

and Wouters[1]. The work of Crochet and Wouters are chosen as the reference for comparison because they have also used a mixed finite elements formulation. The first case focuses on the effects of crystal rotation speeds. The mesh used is a non-uniform grid of 25×51, and it represents half of the crucible. *Figure 18* shows the mesh. The horizontal baffle is placed in the centre of the cylinder. The results for three different rotational Peclet numbers are shown in *Figure 19*.
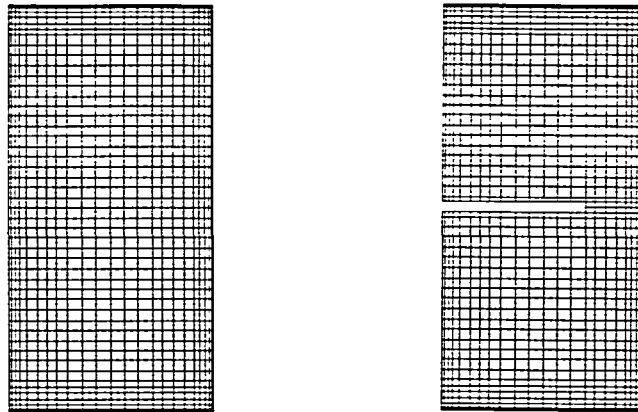
Figure 18 Axisymmetric analysis of heated flow: mesh configuration
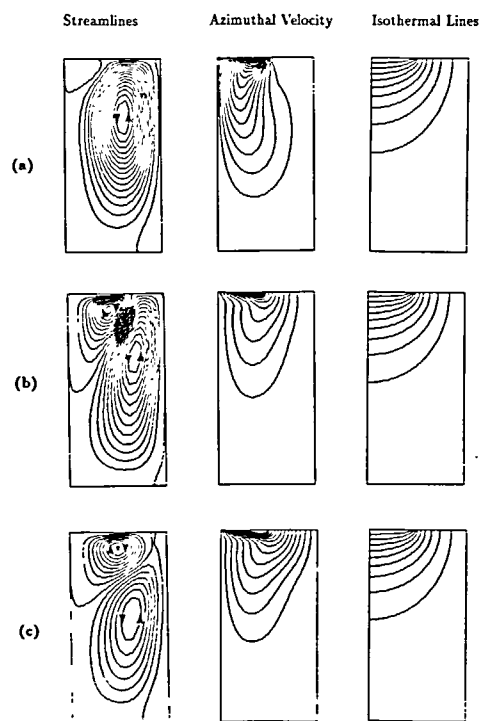
Figure 19 Natural convection and crystal rotation, $Ra = 300$, $Pr = 0.015$; (a) $Pe_s = 5.63$, ($\psi_{max} = 0.06106$, $\psi_{min} = -0.06106$); (b) $Pe_s = 0.01983$, $\psi_{min} = -0.01983$); (c) $Pe_s = 7.95$. ($\psi_{max} = 0.023$, $\psi_{min} = -0.01725$)

The first obvious thing one observes is that the temperature profile remains the same for all three Peclet numbers. However, the Peclet number does have an effect on the velocity profiles. At a low rotation rate, the streamline plot shows one large counter clock circulation that covers most of the cavity, and a small eddy in the upper left corner of the cavity. As the Peclet number increases, the small eddy appears to have increased in size and strength, first taking up half of the crucible, then moving on top of the first circulation. The azimuthal velocity profile also changes as the Peclet number increases. It becomes more spread out and concave towards the axisymmetric line. In general, this behaviour corresponds with the results shown by Crochet and Wouters.

The second case deals with the combined effects of crystal rotation and crucible rotation. *Figure 20* shows the velocity vector, streamline, azimuthal velocity, and isotherms. The crystal and crucible rotation Reynolds numbers used are 500 and 100, respectively. The streamlines show one primary circulation that covers almost the entire cavity, and a small eddy near the corner. These results appear to be consistent with the results of Crochet and Wouters.

The third case deals with the transient natural convection problem. Instead of using the Grashof number as Crochet *et al.*, the Rayleigh number is used in this formulation. For their given Grashof number of 2×10^6 and a Prandtl number of 0.015, the corresponding Rayleigh number is calculated to be 3×10^4. The primary circulation shown in *Figure 21* is at the bottom of the crucible, and its direction is counter clockwise. Furthermore, a plot of the kinetic energy shows that a quasi-steady state is reached at about 4.0 simulated seconds, after which time the kinetic energy oscillates about a certain value.

Finally, the last example investigates the solution for a larger Rayleigh number of 1.5×10^5. Again, the kinetic energy of the system is plotted. As *Figure 23* indicates, a quasi-steady state of oscillating energy is reached in about 4.0 simulated seconds, this time at a higher amplitude and frequency. As the results show in *Figure 22*, at an earlier stage, the streamline plot shows a small circulation between the two larger circulations above and below it. As time advances, this small circulation becomes smaller while the two larger circulations gain more strength and overcome it. The last stage of time in *Figure 22* shows that the small circulation has again returned. This general behaviour is also observed in the Crochet and Wouters' plots.

The results for the axisymmetric flow analysis with baffles are shown in *Figures 24 to 27*. The Rayleigh number used here is 1.771×10^5, and the Prandtl number used is 0.007. As before, g-jitter is varied in frequency and direction. In fact jitter does not have any significant effects on the flow in the case. It is believed that this is due to the action of the rotational motion of the crystal and the crucible. The only favourable result is found in the case with vertical gravity modulation. At $\omega = 20$, vertical jitter, a comparison of the maximum stream function value shows that, the stream function value found for the case with the baffle, shown in *Figure 26*, is
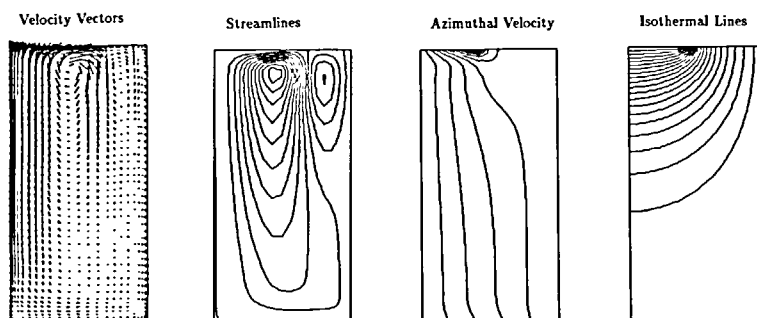
Figure 20 Natural convection, crystal and crucible rotation, $Gr = 2 \times 10^4$, $Pr = 0.015$, $Re_s = 500$, $Re_c = 100$. ($\psi_{max} = 1.0606$, $\psi_{min} = -0.3082$)

Velocity Vectors   Streamlines   Isothermal Lines
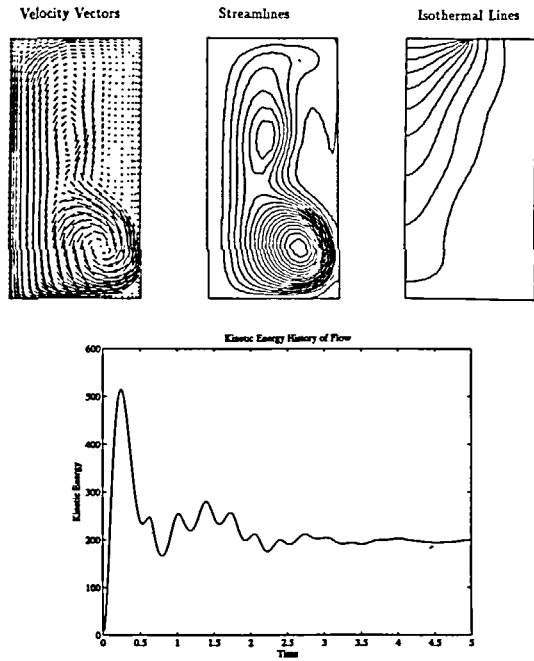

Kinetic Energy History of Flow

Figure 21 Transition from quiescent state to steady state natural convection, $Ra = 3 \times 10^4$, $Pr = 0.015$. $(\psi_{max} = 2.508, \psi_{min} = -2.508)$
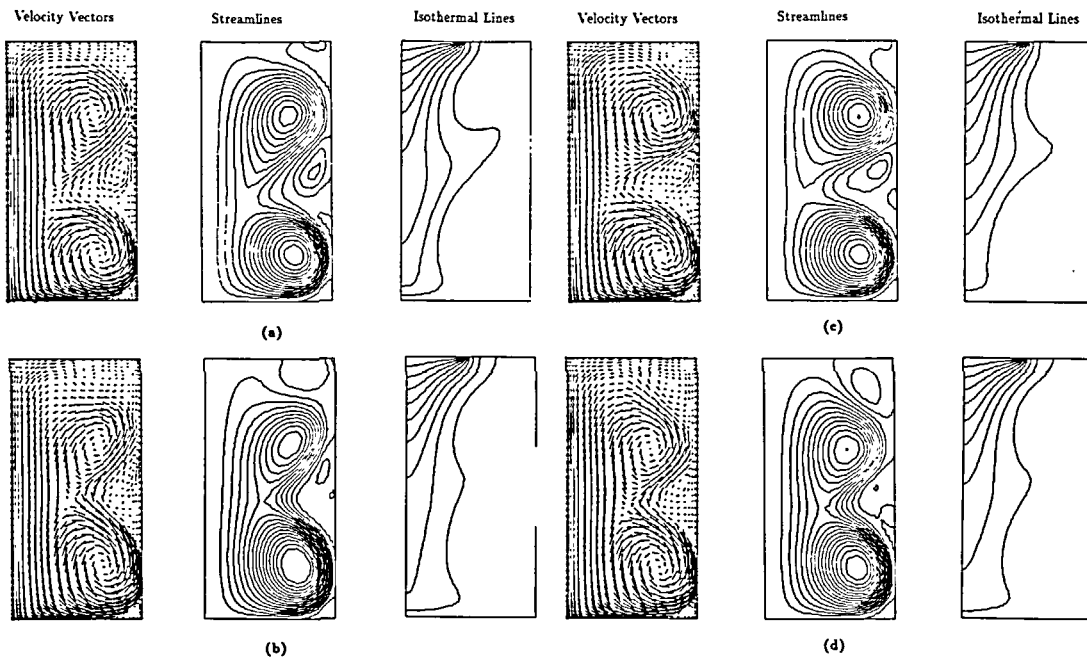
Velocity Vectors   Streamlines   Isothermal Lines   Velocity Vectors   Streamlines   Isothermal Lines

(a)   (c)

(b)   (d)

Figure 22 Velocity vector, streamlines, and isotherms for $Ra = 1.5 \times 10^5$, $Pr = 0.015$; (a) $t = 3.1$, $(\psi_{max} = 5.8525$, $\psi_{min} = -5.8525)$; (b) $t = 3.2$ $(\psi_{max} = 6.689$, $\psi_{min} = -6.689$; (c) $t = 3.5$ $(\psi_{max} = 5.8512$, $\psi_{min} = -5.8512)$; (d) $t = 3.6$ $(\psi_{max} = 6.3396$, $\psi_{min} = -6.3396)$
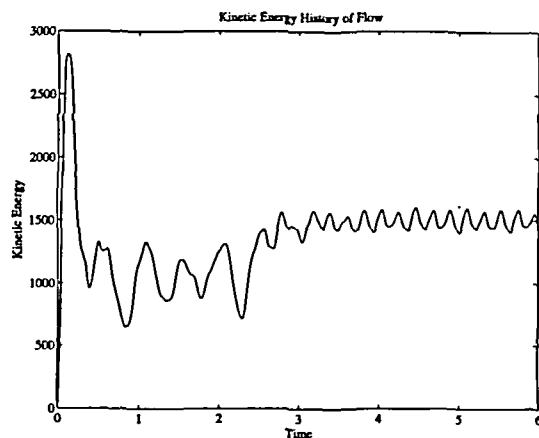
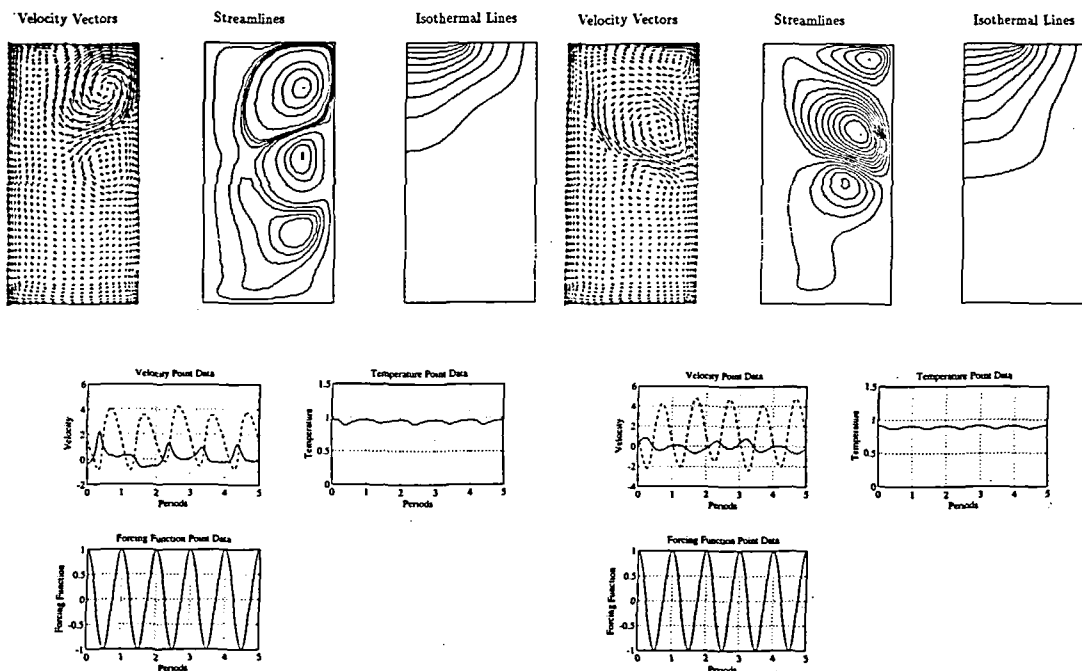*Figure 23* Growth of kinetic energy as a function of time, $Ra = 1.5 \times 10^5$, $Pr = 0.015$

Figure 24 Time-averaged results for $Ra = 1.771 \times 10^5$, $Pr = 0.007$, $\eta = 1.0$, $\omega = 20$, $Pe_c = 7.5$, $Pe_s = 1.5$, $Ar = 0.5$, zero-g, no baffle (vertical jitter). $(\psi_{max} = 0.9964, \psi_{min} = -0.2994)$

Figure 25 Time-averaged results for $Ra = 1.771 \times 10^5$, $Pr = 0.007$, $\eta = 1.0$, $\omega = 40$, $Pe_c = 7.5$, $Pe_s = 1.5$, $Ar = 0.5$, zero-g, no baffle (horizontal jitter). $(\psi_{max} = 0.5353, \psi_{min} = -0.5353)$

almost half of the stream function value for the case without the baffle, shown in *Figure 24*. We therefore conclude that the effects of the baffle on the flow are insignificant when rotational forces are included. Furthermore, the effectiveness of its use depends on its relative direction to the modulation direction.
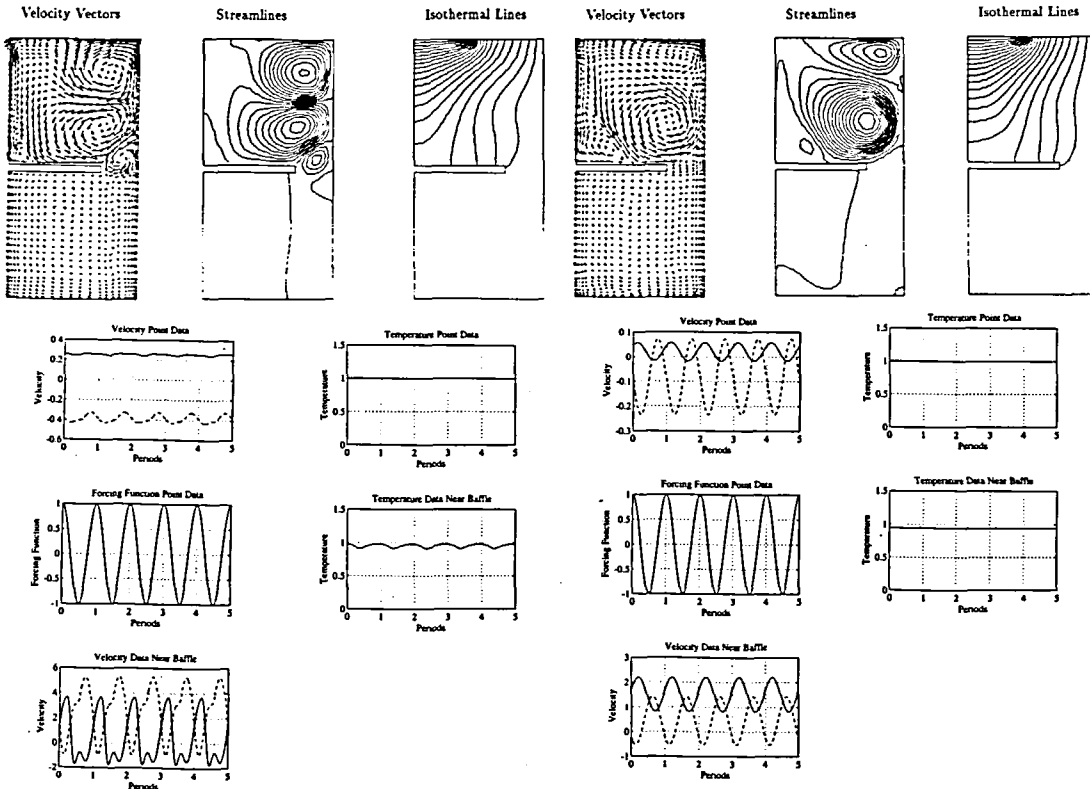
Velocity Vectors   Streamlines   Isothermal Lines   Velocity Vectors   Streamlines   Isothermal Lines

Figure 26   Time-averaged results for $Ra = 1.771 \times 10^5$, $Pr = 0.007$, $\eta = 1.0$, $\omega = 20$, $Pe_c = 7.5$, $Pe_s = 1.5$, $Ar = 0.5$, zero-g, horizontal baffle (vertical jitter). $(\psi_{max} = 0.5198, \psi_{min} = -0.5198)$

Figure 27   Time-averaged results for $Ra = 1.771 \times 10^5$, $Pr = 0.007$, $\eta = 1.0$, $\omega = 40$, $Pe_c = 7.5$, $Pe_s = 1.5$, $Ar = 0.5$, zero-g, horizontal baffle (horizontal jitter). $(\psi_{max} = 0.6495, \psi_{min} = -0.6495)$

CONCLUDING REMARKS

A finite element analysis is performed to study the effects of baffle placement in a heated cavity. The purpose of this study is to learn more about the fluid dynamics and heat transfer mechanism involved in crystal growth from a melt, and whether baffles can be used to suppress the thermal oscillations that is believed to be one of the causes of defects in crystals. The first part of this investigation involves a study of the rectangular cavity flow, and the second part deals with axisymmetric flow analysis for the cylindrical cavity. From the cases studied, the results show that baffles do not induce temperature oscillations, and in some cases, do help to suppress the onset of convection. The best results are obtained when the baffle is placed perpendicular to the g-jitter direction. However, since jitter direction cannot be controlled, and the resulting flow behaviour often depends on the direction of the baffle in relation to the jitter direction, they should not be used in a microgravitational environment. It is recommended that extended future studies be done on this aspect of crystal growth. A better model is needed to include the effects of solid–melt interface interaction, phase change, crystal rotation, pulling, rippling on the free surface, and three-dimensional modelling and analyses of the problem.

ACKNOWLEDGEMENT

REFERENCES

1 Crochet, M. J. and Wouters, P. J. Finite-element simulation of Czochralski bulk flow, *J. Crystal Growth*, **65**, 153–165 (1983)
2 Gresho, P. M. and Sani, R. L. The effects of gravity modulation on the stability of a heat fluid layer, *J. Fluid Mech.*, **40**, 783–806 (1970)
3 Jue, T. C. and Ramaswamy, B. Natural convection with thermocapillary and gravity modulation effects in low-gravity environments, *AIAA J. Spacecraft Rockets*, **29**, 856–869 (1992)
4 Kamotani, Y., Prasad, A. and Ostrach, S. Thermal convection in an enclosure due to vibrations aboard spacecraft, *AIAA J.*, **19**, 511–516 (1981)
5 Sahai, V., Williamson, J. and Overfelt, A. Steady state modeling of large diameter crystal growth using baffles, *Crystal Growth in Space and Related Optical Diagnostics*, **1557**, 60–70 (1991)
6 Whiffen, P. A. C. and Brice, J. C. The suppression of thermal oscillations in Czochralski growth, *J. Crystal Growth*, **10**, 91–96 (1971)